

Article

Petrogenesis and Tectonic Evolution of Huashigou Granitoids in the South Qilian Orogen, NW China: Constraints from Geochronology, Geochemistry, and Sr–Nd–Hf–O Isotopes

Yuxi Wang ^{1,2}, Wanfeng Chen ^{3,*}, Jinrong Wang ⁴, Zhilei Jia ⁵, Qingyan Tang ⁴ and Pengfei Di ⁶

- ¹ Gold Mine Resource Exploration and Utilization Technology Innovation Center of Gansu Province, Lanzhou 730050, China; wangyx15@lzu.edu.cn
 - ² The Third Institute of Geology and Minerals Exploration, Gansu Provincial Bureau of Geology and Minerals Exploration and Development, Lanzhou 730050, China
 - ³ College of Geography and Tourism, Hunan University of Arts and Science, Changde 415000, China
 - ⁴ Key Laboratory of Mineral Resources in Western China, School of Earth Sciences, Lanzhou University, Lanzhou 730000, China; jrwang@lzu.edu.cn (J.W.); tangqy@lzu.edu.cn (Q.T.)
 - ⁵ Gansu Provincial Bureau of Geology and Mineral Exploration and Development, Lanzhou 730000, China; kaka20100502@outlook.com
 - ⁶ Gansu Assessment Center of Mineral Resources Reserves, Lanzhou 730000, China; dipf15@lzu.edu.cn
- * Correspondence: chenwanfeng@huas.edu.cn

Abstract: The origin of granitic rocks from the South Qilian orogenic belt is of great significance for understanding the continental tectonic framework of Western China. Currently, scholars have different opinions on the tectonic evolution of the South Qilian. Huashigou granite, which exhibits multiple intrusive episodes, is a suitable example for studying the tectonic evolution of the South Qilian. New zircon U–Pb ages and the whole-rock elemental and Sr–Nd–Hf–O isotopic compositions of Huashigou granitic rocks are presented here to investigate their petrogenesis and discuss the tectonic implications for the evolution of the South Qilian orogenic belt. LA-ICP-MS zircon U–Pb dating yielded crystallization ages of 368.7 ± 3.5 Ma, 261.5 ± 0.63 Ma, and 262.2 ± 1.4 Ma for granodiorites from the Hua1 pluton, quartz diorites from the Hua2 pluton, and porphyritic tonalites from the Hua4 pluton, respectively. Late Devonian granodiorites from the Hua1 pluton belonged to the metaluminous calc-alkaline series and were characterized by an enrichment in LREEs, a depletion in HREEs, negative Eu anomalies, and Sr/Y ratios of 9.17 to 11.67. They showed $(^{87}\text{Sr}/^{86}\text{Sr})_i$ ratios of 0.712356 to 0.71195, $\epsilon_{\text{Nd}}(t)$ values of -6.56 to -6.14 , and an $\epsilon_{\text{Hf}}(t)$ value of -2.06 . Middle Permian granitic rocks mainly consisted of quartz diorites and porphyritic tonalites, which are part of the metaluminous tholeiitic series and weakly peraluminous tholeiitic series, respectively. Quartz diorites from the Hua2 pluton were characterized by an enrichment in LREEs, depletions in HREEs and HESEs, weak negative Eu anomalies, and Sr/Y ratios of 13.25 to 14.79. They showed $(^{87}\text{Sr}/^{86}\text{Sr})_i$ ratios of 0.705905 to 0.705971, $\epsilon_{\text{Nd}}(t)$ values of $+0.78$ to $+0.82$, and a $\delta^{18}\text{O}_{\text{V-SMOW}}$ value of 12.4‰. Porphyritic tonalites of the Hua4 pluton were characterized by an enrichment in LREEs, depletions in HREEs and HESEs, weak negative Eu anomalies, and Sr/Y ratios of 9.22 to 12.74. They showed $(^{87}\text{Sr}/^{86}\text{Sr})_i$ ratios of 0.719528, $\epsilon_{\text{Nd}}(t)$ values of -8.57 , and a $\delta^{18}\text{O}_{\text{V-SMOW}}$ value of 11.8‰. We can conclude that Late Devonian granodiorites were derived from the partial melting of enriched and shallow-depth crustal materials, whereas Middle Permian granitic rocks were formed by the delamination of a thickened lower crust after the closure of the Paleo-Tethys Ocean, which caused the underplating of mantle-derived basaltic magma, inducing the partial melting of the lower crust at different depths. Our results show that there were at least two important stages of compressional and extensional tectonic switches in the South Qilian orogenic belt during the Late Paleozoic Era, and the evolution of Altyn Tagh–Qilian–North Qaidam had evident stages.

Keywords: granitoids; geochemistry; Sr–Nd–Hf–O isotopes; tectonic evolution; Qilian orogenic belt



Citation: Wang, Y.; Chen, W.; Wang, J.; Jia, Z.; Tang, Q.; Di, P. Petrogenesis and Tectonic Evolution of Huashigou Granitoids in the South Qilian Orogen, NW China: Constraints from Geochronology, Geochemistry, and Sr–Nd–Hf–O Isotopes. *Minerals* **2024**, *14*, 71. <https://doi.org/10.3390/min14010071>

Academic Editors: Jaroslav Dostal, Jiafu Chen, Nan Ju and Zhonghai Zhao

Received: 20 October 2023
Revised: 15 December 2023
Accepted: 18 December 2023
Published: 6 January 2024



Copyright: © 2024 by the authors. Licensee MDPI, Basel, Switzerland. This article is an open access article distributed under the terms and conditions of the Creative Commons Attribution (CC BY) license (<https://creativecommons.org/licenses/by/4.0/>).

1. Introduction

The Qilian orogenic belt, located at the northeastern margin of the Tibetan Plateau, is located in the western part of the central orogenic belt that runs across China from east to west [1–5]. The Qaidam Block is located to the south of the belt. The Tarim Craton is located northwest of the belt, delineated by the Altyn Tagh Fault (Figure 1a). A majority of studies have been conducted to investigate the evolution of the Altyn Tagh–Qilian–North Qaidam tectonic system [6–27]. These studies focus on the discovery of an ultrahigh-pressure metamorphic belt (UHPB) in the North Qaidam and Altyn Tagh regions and its comparison to the Altyn Tagh–Qilian–North Qaidam tectonic system [3,28–33]. As a ubiquitous intrusive mass in the orogenic belt, granitoids have recorded much information about plate tectonics and crustal evolution [12,34–40]. Additionally, there are similarities between the tectonic units on both sides of Altyn Tagh.

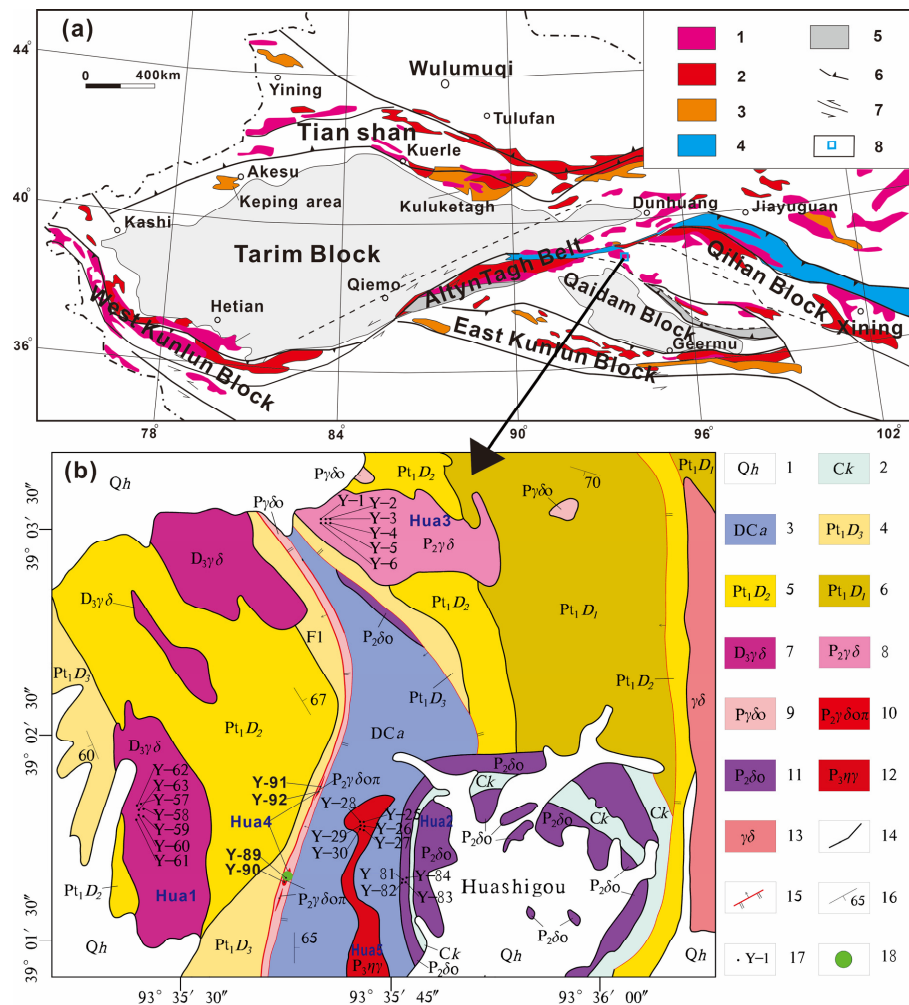


Figure 1. Tectonic location (a) and geological sketch map (b) of the South Qilian Orogen. (a): 1. Archean–Paleoproterozoic basement; 2. Mesoproterozoic rock; 3. Neoproterozoic rock; 4. Early Paleozoic subduction collision complex belt; 5. Early Paleozoic subduction hyperplasia complex belt; 6. thrust fault; 7. strike-slip fault; and 8. study area. (b): 1. Quaternary; 2. Carboniferous Yanghugou Group; 3. Devonian–Carboniferous Amunike Group; 4. Paleoproterozoic Dakendaban Group (the Third Rock Group); 5. Paleoproterozoic Dakendaban Group (the Second Rock Group); 6. Paleoproterozoic Dakendaban Group (the First Rock Group); 7. Late Devonian granodiorites (Hua1); 8. Middle Permian granitoids (Hua3); 9. quartz mica diorites; 10. Middle Permian quartz mica porphyritic diorites (Hua4); 11. Middle Permian quartz diorites (Hua2); 12. Late Permian monzogranites (Hua5); 13. granodiorites; 14. geological boundary; 15. faults; 16. attitude; 17. sample locations; and 18. copper deposits.

Previous studies have mainly focused on Early Paleozoic granitic rocks in the North Qilian orogenic belt, while studies on Late Paleozoic granitoids are relatively scarce. Since the closure of the Qilian orogenic belt in the Mid–Late Paleozoic, there has been a paucity of pertinent research findings. Consequently, Late Paleozoic granitic rocks serve as a pivotal means to unveil not only their geodynamic implications but also the geological evolution of the Qilian orogenic belt.

In this study, we present results from petrographic, geochronologic, and whole-rock elemental and Sr–Nd–Hf–O isotopic composition analyses in an attempt to investigate the petrogenesis of Paleozoic Huashigou granitoids in the South Qilian along the northeastern margin of the Tibetan Plateau. These data could be used to infer and determine the age, genesis, and tectonic environment of the rocks formed during that period in the South Qilian. The data were used to evaluate the crustal evolution of the Qilian Orogen in the Late Paleozoic.

2. Regional Geology and Petrography

The Huashigou area is located at the southwest margin of the Qilian Orogen, which is at the junction of the Altyn Tagh–Qilian–North Qaidam tectonic belt. Paleoproterozoic (Dakendaban Group), Devonian (Amunike Formation), and Carboniferous (Kelukue Formation) strata are widely distributed in the study area. The Paleoproterozoic Dakendaban Group represents a major stratigraphic formation developed in this area. The Devonian and Carboniferous strata are mainly distributed at the center of the study area. Faults extend in the north–south and north–west directions. The Huashigou area consists of five types of granitic rocks, including granodiorite, biotite granodiorite, porphyritic tonalite, quartz diorite, and monzonitic granite (Figure 1b).

Three granodiorite intrusions exist, with sizes ranging from 2 to 0.1 km², which intruded into Paleoproterozoic metamorphic rocks (Dakendaban Group). The Hua1 pluton is composed of plagioclase (47%), quartz (20%), albite (18%), biotite (10%), hornblende (5%), and accessory minerals, including apatite, zircon, sphene, and magnetite. Plagioclases are wide and tabular and are intensively altered, with sericitization, decarbonation, and clayzation alterations. Some plagioclase grains wrapped in microcline have an obvious albite reaction rim. Quartzes are in a xenomorphic–granular form, and some of them show wavy extinction in rare situations.

The Hua2 pluton is mainly located south of the study area, with extensive exposure intruding in the Paleoproterozoic Dakendaban Group and Carboniferous Kelukue Group, with a long strip layout and small areas in general. The pluton exhibits a subhedral–granular texture and a blocky structure and consists of plagioclase (70%), normal hornblende (15%), quartz (10%), and biotite (5%), with minor accessory minerals, including apatite, zircon, sphene, and magnetite. Plagioclases are mainly tabular and dotted with small amounts of secondary minerals, such as clay, microcryptocrystalline zoisite, sericite, and carbonates. Hornblende is intensively altered, with actinolitization along fractures.

The Hua3 pluton is located north of the study area, covering about 2 km² in a nearly elliptical shape. With a fine-grained granite texture, the pluton mainly has a blocky structure and is composed of plagioclase (49%), orthoclase (15%), quartz (18%), biotite (15%), microcline (3%), and accessory minerals, including apatite, zircon, and magnetite. The tabular biotite is slightly wrapped in orthoclase, and the plagioclase has a visible polysynthetic twin and a mostly rapakivi structure. LA-ICP-MS zircon U–Pb dating indicated that the pluton was emplaced in the Middle Permian (261.1 ± 3.8 Ma [41]).

The irregular zonal Hua4 pluton is mainly distributed along the F1 Fault. The pluton shows typical porphyritic textures, and its phenocrysts include plagioclase and quartz. Its groundmass is composed of plagioclase, quartz, sericite, and biotite, with microgranular, cataclastic, and blocky structures. The plagioclase phenocrysts are in lenticular and elliptical shapes, and some parts have a wide tabular shape, with particle sizes ranging from 0.6 to 1.0 mm. Quartz phenocrysts have an elliptical shape, aggregating along the fractures with a sericite particle size of ± 1.0 mm.

The Hua5 pluton intruded into the Devonian Amunike *Group*, with an exposed surface area of about 0.4 km². The pluton displays a fine-grained granitic and blocky structure and consists of plagioclase (45%), quartz (23%), biotite (12%), perthite (12%), microcline (7%), and minor accessory minerals, such as apatite, sphene, zircon, and magnetite. LA-ICP-MS zircon U–Pb dating indicated that the pluton was formed in the Late Permian (252.0 ± 2.1 Ma [42]).

3. Analytical Methods

Sixteen samples were collected from the granitic plutons in the Huashigou area, including seven from the Hua1 pluton (YQ57–YQ63), four from the Hua2 pluton (YQ81–84), and four from the Hua4 pluton (YQ89–92). The locations of the analyzed samples are shown in Figure 1b.

3.1. Zircon U–Pb Age Analytical Method

Firstly, zircon grains were separated using conventional magnetic techniques and handpicked using a binocular microscope (BX51, Olympus, Tokyo, Japan). The zircon grains were mounted in an epoxy mount and polished down to a half-section. Prior to the isotope analysis, all grains were photographed under transmitted and reflected light and subsequently examined using cathode luminescence (CL) images (JSM-6510, JEOL, Tokyo, Japan). The zircon LA-ICP-MS U–Pb analyses were performed on a 7500 ICP-MS (Agilent, Santa Clara, CA, USA) with a UP193SS LA (New Wave, Seattle, WA, USA) at the Key Laboratory of Lithospheric Tectonics and Exploration of the Ministry of Education, China University of Geosciences (Beijing), China. The samples were analyzed in runs, with four GJ-1 zircon standards measured every ten to twelve samples. The analytical data were then reduced, calculated, and plotted using the Squid 1.0 and Isoplot programs (version 4.00.08.09.16, by KR Ludwig, Berkeley Geochr. Ctr., Berkeley, CA, USA) [43]. The compositions of common Pbs were corrected following the Andersen method [44]. Errors during the individual analyses are cited at 1σ, and the weighted age uncertainties are quoted at a confidence level of 95%.

3.2. Whole-Rock, Sr–Nd–O, and Hf Isotopic Analytical Method

The whole-rock major elements, trace elements, and Sr–Nd–Hf isotopes were determined at the State Key Laboratory of Continental Dynamics, Northwest University, China. The samples for the whole-rock chemical analysis were crushed to 200 mesh. The major-element contents of the samples were analyzed using the RIX-2100 (RIGAKU, Tokyo, Japan) X-ray fluorescence spectrometer (XRF). The analytic uncertainties were generally less than 2% for most of the major elements and 2% to 5% for the major elements with <1 wt.% contents. Trace elements and rare-earth elements (REEs) were analyzed using the Elan-6100DRC model ICP-MS (Perkin Elmer, Waltham, MA, USA). About 50 mg of the powder samples was dissolved in high-pressure Teflon bombs using a HF + HNO₃ mixture. The analytical precision was better than 5%. The Nd, Sr, and Hf isotopic analyses were performed using MC-ICP-MS (Nu Instruments, North Wales, UK), and the isotopic ratios were, respectively, normalized to ¹⁴³Nd/¹⁴⁴Nd = 0.7219, ⁸⁷Sr/⁸⁶Sr = 8.3721, and ¹⁷⁶Hf/¹⁷⁷Hf = 0.7325. The oxygen-stable isotopes of the whole-rock samples were determined at the Institute of Mineral Resources, Chinese Academy of Geological Science (Beijing, China). The oxygen isotopic compositions (δ¹⁸O) were analyzed using the BrF₅ method and measured using the MAT-253 mass spectrometer (MAT-253, Thermo Fisher Scientific, Waltham, MA, USA), according to international standards (SMOW), with a precision of ±0.2 ‰.

4. Results

Fifteen samples were collected for the major- and trace-element analyses, of which three samples were used for zircon U–Pb dating, six samples were used for Sr–Nd isotopic analyses, one sample was used for Hf isotopic analyses, and two samples were used for O isotopic analyses. The detailed data are presented in Tables 1–3.

Table 1. Major- and trace-element compositions of Huashigou granitoids.

Lithology	Hua1						Hua2						Hua4		
Sample	YQ-57	YQ-58	YQ-59	YQ-60	YQ-61	YQ-62	YQ-63	YQ-81	YQ-82	YQ-83	YQ-84	YQ-89	YQ-90	YQ-91	YQ-92
<i>Major elements (%)</i>															
SiO ₂	67.78	68.48	67.81	68.87	68.16	68.35	68.44	52.41	53.32	52.43	52.54	67.28	66.43	63.64	67.01
TiO ₂	0.41	0.40	0.48	0.42	0.44	0.42	0.41	1.58	1.40	1.57	1.57	0.50	0.49	0.55	0.48
Al ₂ O ₃	15.77	15.29	15.43	15.26	15.41	15.52	15.45	19.69	19.66	19.67	19.68	16.07	16.34	16.62	16.18
TFe ₂ O ₃	3.69	3.62	4.01	3.67	3.83	3.68	3.60	9.23	8.71	9.01	8.91	3.95	3.83	4.34	3.72
MnO	0.06	0.06	0.06	0.06	0.06	0.06	0.06	0.09	0.11	0.09	0.09	0.03	0.04	0.06	0.04
MgO	1.22	1.19	1.38	1.20	1.31	1.25	1.21	3.18	2.99	3.25	3.14	1.81	1.73	2.50	2.09
CaO	3.80	3.48	3.72	3.39	3.65	3.66	3.56	8.07	7.97	8.11	7.91	1.65	2.08	2.93	1.82
Na ₂ O	3.79	3.60	3.53	3.57	3.65	3.68	3.65	4.81	4.75	4.91	4.77	4.13	4.39	3.50	4.41
K ₂ O	2.71	3.06	2.83	3.06	3.02	2.99	3.01	0.64	0.63	0.65	0.68	3.77	3.63	3.80	3.61
P ₂ O ₅	0.11	0.13	0.15	0.13	0.14	0.13	0.13	0.23	0.24	0.24	0.22	0.14	0.14	0.12	0.14
LOI	0.95	0.90	0.94	0.82	0.61	0.67	0.77	0.31	0.54	0.34	0.29	0.95	1.06	1.47	0.86
TOTAL	100.29	100.21	100.34	100.45	100.28	100.41	100.29	100.24	100.32	100.27	99.8	100.28	100.16	99.53	100.36
Mg [#]	37.24	37.10	38.18	36.98	38.03	37.87	37.62	38.20	38.12	39.29	38.74	45.12	44.77	50.83	50.20
A/CNK	1.07	1.05	1.07	1.06	1.04	1.05	1.05	1.06	1.07	1.04	1.07	1.15	1.11	1.12	1.13
<i>Trace elements (×10⁻⁶)</i>															
Rb	90.18	105.55	95.42	107.30	106.60	105.01	105.51	16.78	17.93	16.61	18.61	146.57	140.96	190.47	164.27
Cs	2.44	2.92	2.50	3.15	3.44	3.31	3.36	0.88	0.89	0.87	0.91	4.52	4.31	6.09	5.11
Sr	226.50	211.00	218.50	205.30	210.30	213.10	210.50	585.70	573.90	584.60	593.10	172.40	197.90	217.30	194.90
Ba	690.00	702.30	777.70	685.20	700.70	679.20	666.00	191.40	177.60	194.00	203.50	1066.10	993.00	1015.30	1103.40
Sc	7.81	8.08	9.25	8.28	8.77	8.01	8.23	27.04	24.30	27.61	25.72	10.40	10.62	9.33	10.30
Nb	14.02	14.82	16.40	15.90	15.31	14.68	14.69	11.41	11.29	11.34	11.80	13.81	13.30	13.59	13.18
Ta	0.98	1.11	1.14	1.28	1.10	1.14	1.08	0.53	0.60	0.55	0.57	1.00	1.00	0.93	0.95
Zr	196.99	200.86	195.42	194.65	223.69	192.78	230.61	213.65	227.58	215.93	194.50	171.99	184.44	143.45	155.80
Hf	4.82	5.08	4.91	5.04	5.66	4.89	5.72	4.86	5.23	4.91	4.42	4.42	4.70	3.64	4.07
U	1.59	1.62	1.75	1.61	1.50	1.46	1.89	0.54	0.77	0.58	0.44	3.48	3.02	2.50	1.85
Th	13.76	19.08	18.32	20.48	18.26	17.15	19.12	2.59	2.59	2.41	2.99	14.53	16.05	9.89	13.48
Cr	7.12	7.69	8.68	6.81	7.53	7.16	6.70	5.25	3.67	4.14	5.07	13.32	10.51	9.50	10.30
Ni	6.15	6.34	7.21	5.88	6.47	6.20	6.15	8.80	6.65	7.46	9.45	11.71	10.71	11.99	9.59
La	39.88	47.78	49.15	55.70	51.45	41.47	48.44	22.45	21.54	22.81	24.04	35.27	43.04	39.44	28.11
Ce	71.71	83.73	90.00	99.07	89.04	73.19	84.75	56.02	55.19	56.33	56.94	61.80	72.08	64.31	49.20
Pr	7.01	8.53	8.96	9.72	8.97	7.48	8.42	7.93	8.01	8.00	7.88	6.44	7.44	6.40	5.17
Nd	23.53	28.52	30.33	32.69	30.10	25.57	28.36	36.66	38.06	36.75	35.55	22.45	25.07	22.19	18.42
Sm	3.92	4.70	5.06	5.20	4.90	4.39	4.60	8.63	9.04	8.74	8.27	3.89	4.19	3.65	3.37
Eu	1.09	1.04	1.11	1.03	1.07	1.05	1.04	2.40	2.36	2.42	2.37	0.82	0.95	1.58	0.82
Gd	3.58	4.23	4.55	4.59	4.36	4.04	4.12	8.43	8.67	8.60	8.10	3.45	3.83	3.27	3.20
Tb	0.53	0.62	0.67	0.67	0.64	0.60	0.60	1.30	1.35	1.33	1.25	0.52	0.57	0.46	0.50
Dy	3.25	3.74	4.04	3.99	3.78	3.65	3.57	7.79	7.96	7.94	7.44	3.13	3.46	2.66	3.11
Ho	0.65	0.75	0.80	0.80	0.76	0.74	0.73	1.54	1.59	1.57	1.48	0.64	0.70	0.55	0.65
Er	1.91	2.24	2.36	2.41	2.27	2.18	2.13	4.32	4.45	4.37	4.13	1.92	2.10	1.72	1.91
Tm	0.30	0.35	0.37	0.38	0.35	0.35	0.34	0.62	0.64	0.62	0.59	0.30	0.33	0.28	0.30
Yb	1.99	2.32	2.42	2.49	2.33	2.29	2.23	3.75	3.97	3.77	3.62	2.03	2.15	2.01	1.95
Lu	0.31	0.36	0.37	0.38	0.36	0.35	0.35	0.55	0.58	0.55	0.52	0.32	0.34	0.33	0.30
Y	19.41	22.74	23.82	24.23	22.90	22.25	21.88	42.36	43.32	42.57	40.10	18.71	20.98	17.05	19.87
∑REE	569.67	672.88	708.91	765.86	708.83	606.44	670.30	701.28	710.84	708.67	692.53	519.60	600.28	543.21	441.35
(La/Yb) _N	14.39	14.77	14.59	16.05	15.82	12.97	15.56	4.29	3.89	4.33	4.77	12.46	14.39	14.09	10.33
δEu	0.89	0.72	0.71	0.64	0.71	0.76	0.73	0.86	0.82	0.85	0.89	0.68	0.72	1.40	0.76

Note: The contents of major elements, REEs, and trace elements were analyzed at the State Key Laboratory of Continental Dynamics, Northwest University. An XRF analysis was adopted to analyze major elements, and the experimental instrument used (RIX2100) was manufactured by the Japanese company RIGAKU. Trace elements were analyzed and graded using the Elan6100DRC model ICP-MS, supplied by Perkin Elmer, an American-based company. The relative error and relative standard deviation of the majority of elements were less than 5%.

Table 2. Sr–Nd–Hf–O isotopic compositions of Huashigou granites.

Sample	⁸⁷ Sr/ ⁸⁶ Sr	2s	Sr (×10 ⁻⁶)	Rb (×10 ⁻⁶)	⁸⁶ Sr (×10 ⁻⁶)	⁸⁷ Rb/ ⁸⁶ Sr	(⁸⁷ Sr/ ⁸⁶ Sr) _i	U–Pb Age/Ga		
YQ-57	0.718408	0.000121	227	90.2	0.0985	1.153	0.712356	0.3687		
YQ-63	0.719577	0.000114	210	106	0.0985	1.452	0.711936	0.3687		
YQ-83	0.706211	0.000018	585	16.6	0.0986	0.082	0.705905	0.2618		
YQ-84	0.706309	0.000023	593	18.6	0.0986	0.091	0.705971	0.2618		
YQ-91	0.729009	0.000021	217	190	0.0984	2.542	0.719528	0.2622		
YX-1	0.732882	0.000124	144	154	0.0984	3.094	0.721339	0.2622		

Sample	¹⁴³ Nd/ ¹⁴⁴ Nd	2s	Nd (×10 ⁻⁶)	Sm (×10 ⁻⁶)	¹⁴⁴ Nd (×10 ⁻⁶)	¹⁴⁷ Sm/ ¹⁴⁴ Nd	(¹⁴³ Nd/ ¹⁴⁴ Nd) _i	ε _{Nd} (t)	T _{2DM} (Ga)	t _{CHUR} (Ga)
YQ-57	0.512070	0.000013	23.5	3.92	0.2380	0.1006	0.511827	-6.555202	1.6	0.900661
YQ-63	0.512068	0.000007	28.4	4.60	0.2380	0.9080	0.511815	-6.790724	1.6	0.905239
YQ-83	0.512587	0.000008	36.7	8.74	0.2380	0.1437	0.512341	0.778167	1.0	0.146910
YQ-84	0.512584	0.000007	35.6	8.27	0.2380	0.1406	0.512343	0.824325	1.0	0.146764
YQ-91	0.512032	0.000006	22.2	3.65	0.2380	0.0993	0.511861	-8.569046	1.7	0.948493
YX-1	0.512072	0.000006	29.2	4.83	0.2380	0.1001	0.511899	-7.817007	1.7	0.893627

Sample	¹⁷⁶ Hf/ ¹⁷⁷ Hf	2s	Lu (×10 ⁻⁶)	Hf (×10 ⁻⁶)	¹⁷⁷ Hf (×10 ⁻⁶)	¹⁷⁶ Hf (10 ⁻⁶)	¹⁷⁶ Lu	¹⁷⁶ Lu/ ¹⁷⁷ Hf	(¹⁷⁶ Hf/ ¹⁷⁷ Hf) _i	ε _{Hf} (t)	T _{DM} (Ga)
YQ-83	0.282543	0.000009	0.35	5.72	0.185953	0.052604	0.02584	0.0084777	0.28248	-2.07584	1.4

Sample	Lithology
YQ-83	Quartz diorite
YQ-91	Quartz mica porphyritic diorite

Note: The Sr–Nd–Hf isotopic compositions were analyzed at the State Key Laboratory of Continental Dynamics, Northwest University, while the composition of oxygen isotopes (δ¹⁸O) was determined at the Institute of Mineral Resources, Chinese Academy of Geological Science.

Table 3. LA-ICP-MS U–Pb zircon data of Huashigou granites.

Spots	²³⁸ U (×10 ⁻⁶)	²³² Th (×10 ⁻⁶)	Th/U	Isotope Ratio						Isotope Age			
				²⁰⁶ Pb/ ²³⁸ U	1σ	²⁰⁷ Pb/ ²³⁵ U	1σ	²⁰⁷ Pb/ ²⁰⁶ Pb	1σ	²⁰⁶ Pb/ ²³⁸ U	1σ	²⁰⁷ Pb/ ²³⁵ U	1σ
YQ57-01	315	190	0.60	0.05889	0.00087	0.48024	0.01794	0.05914	0.00222	369	5	398	12
YQ57-02	350	116	0.33	0.06042	0.00088	0.43998	0.01578	0.05280	0.0019	378	5	370	11
YQ57-03	150	97	0.65	0.06003	0.00108	0.46993	0.03886	0.05678	0.00481	376	7	391	27
YQ57-05	316	274	0.87	0.05920	0.00087	0.46580	0.01765	0.05706	0.00217	371	5	388	12
YQ57-06	339	224	0.66	0.05871	0.00087	0.42920	0.01595	0.05301	0.00198	368	5	363	11
YQ57-07	252	232	0.92	0.06073	0.00090	0.47908	0.01839	0.05721	0.00221	380	5	397	13
YQ57-08	355	326	0.92	0.05921	0.00087	0.43751	0.01630	0.05359	0.00201	371	5	368	12
YQ57-09	293	223	0.76	0.05810	0.00086	0.45036	0.01849	0.05621	0.00232	364	5	378	13
YQ57-12	361	204	0.56	0.06005	0.00089	0.48010	0.01811	0.05798	0.00220	376	5	398	12
YQ57-13	439	288	0.66	0.05781	0.00085	0.42800	0.01604	0.05369	0.00202	362	5	362	11
YQ57-15	284	195	0.69	0.06071	0.00091	0.45580	0.01880	0.05445	0.00226	380	6	381	13
YQ57-16	348	297	0.85	0.05931	0.00089	0.47418	0.01820	0.05798	0.00224	371	5	394	13
YQ57-17	290	173	0.60	0.05908	0.00091	0.43250	0.01788	0.05308	0.00222	370	6	365	13
YQ57-18	427	293	0.69	0.05886	0.00088	0.44790	0.01736	0.05518	0.00215	369	5	376	12
YQ57-19	273	157	0.57	0.05829	0.00088	0.46156	0.01955	0.05742	0.00245	365	5	385	14
YQ57-20	440	415	0.94	0.05592	0.00084	0.45384	0.01804	0.05886	0.00236	351	5	380	13
YQ57-21	404	259	0.64	0.05727	0.00086	0.43694	0.01781	0.05533	0.00227	359	5	368	13
YQ57-22	413	271	0.66	0.05881	0.00088	0.43850	0.01720	0.05407	0.00214	368	5	369	12
YQ57-23	162	108	0.67	0.05978	0.00094	0.47134	0.02617	0.05717	0.00320	374	6	392	18
YQ57-25	330	230	0.70	0.05761	0.00090	0.42060	0.01812	0.05295	0.00231	361	5	356	13
YQ81-01	177	153	0.86	0.04155	0.00062	0.29453	0.01115	0.05141	0.00196	262	4	262	9
YQ81-02	239	228	0.95	0.04167	0.00060	0.29783	0.01107	0.05183	0.00193	263	4	265	9
YQ81-03	236	281	1.19	0.04182	0.00061	0.29759	0.01127	0.05161	0.00196	264	4	265	9
YQ81-04	99	72	0.73	0.04197	0.00066	0.29891	0.01434	0.05165	0.00250	265	4	266	11
YQ81-05	151	123	0.81	0.04105	0.00061	0.29311	0.01254	0.05178	0.00223	259	4	261	10
YQ81-06	217	204	0.94	0.04174	0.00061	0.30703	0.01496	0.05335	0.00260	264	4	272	12
YQ81-07	86	62	0.72	0.04313	0.00069	0.30454	0.02352	0.05120	0.00397	272	4	270	18
YQ81-08	149	121	0.81	0.04087	0.00062	0.28327	0.01129	0.05026	0.00202	258	4	253	9
YQ81-09	49	17	0.35	0.04204	0.00075	0.29870	0.02003	0.05152	0.00349	265	5	265	16
YQ81-10	150	129	0.86	0.04095	0.00062	0.29902	0.01291	0.05295	0.00230	259	4	266	10
YQ81-11	136	82	0.60	0.04043	0.00062	0.28644	0.01301	0.05138	0.00235	255	4	256	10
YQ81-12	120	103	0.85	0.04057	0.00065	0.28818	0.01395	0.05151	0.00252	256	4	257	11
YQ81-13	135	113	0.84	0.04076	0.00063	0.29006	0.01336	0.05161	0.00240	258	4	259	11
YQ81-14	125	108	0.87	0.04255	0.00066	0.30327	0.01373	0.05169	0.00236	269	4	269	11
YQ81-15	105	87	0.82	0.04228	0.00068	0.31220	0.01887	0.05355	0.00326	267	4	276	15
YQ81-16	159	136	0.85	0.04097	0.00064	0.29132	0.01328	0.05156	0.00237	259	4	260	10
YQ81-17	130	126	0.97	0.04318	0.00067	0.29919	0.01248	0.05024	0.00212	273	4	266	10
YQ81-18	175	148	0.85	0.04153	0.00062	0.29472	0.01278	0.05146	0.00224	262	4	262	10
YQ81-19	154	131	0.85	0.03991	0.00061	0.28186	0.01182	0.05122	0.00216	252	4	252	9
YQ81-20	161	140	0.87	0.04046	0.00062	0.29061	0.01533	0.05209	0.00276	256	4	259	12
YQ81-21	125	97	0.77	0.04172	0.00066	0.29840	0.01384	0.05187	0.00243	263	4	265	11
YQ81-22	117	102	0.87	0.04233	0.00066	0.30153	0.01521	0.05166	0.00263	267	4	268	12
YQ81-23	55	18	0.32	0.03984	0.00075	0.28010	0.03220	0.05099	0.00589	252	5	251	26
YQ81-24	114	89	0.78	0.04082	0.00066	0.28811	0.01330	0.05119	0.00239	258	4	257	10

Table 3. Cont.

Spots	²³⁸ U (×10 ⁻⁶)	²³² Th (×10 ⁻⁶)	Th/U	Isotope Ratio						Isotope Age			
				²⁰⁶ Pb/ ²³⁸ U	1σ	²⁰⁷ Pb/ ²³⁵ U	1σ	²⁰⁷ Pb/ ²⁰⁶ Pb	1σ	²⁰⁶ Pb/ ²³⁸ U	1σ	²⁰⁷ Pb/ ²³⁵ U	1σ
YQ81-25	40	16	0.40	0.03988	0.00083	0.28361	0.03353	0.05157	0.00614	252	5	254	27
YQ81-26	83	32	0.38	0.04179	0.0007	0.29816	0.01652	0.05175	0.00290	264	4	265	13
YQ81-27	100	83	0.83	0.04162	0.00067	0.29657	0.01594	0.05168	0.00280	263	4	264	12
YQ81-28	135	115	0.86	0.04160	0.00065	0.29434	0.01348	0.05131	0.00237	263	4	262	11
YQ81-29	76	53	0.70	0.04171	0.00073	0.29603	0.01754	0.05147	0.00309	263	5	263	14
YQ81-30	141	129	0.91	0.04253	0.00067	0.30127	0.01447	0.05138	0.00249	268	4	267	11
YQ81-31	195	179	0.92	0.04061	0.00062	0.28495	0.01207	0.05088	0.00217	257	4	255	10
YQ81-32	234	210	0.90	0.04081	0.00061	0.28668	0.01135	0.05095	0.00203	258	4	256	9
YQ81-33	49	20	0.40	0.04214	0.00079	0.29406	0.02197	0.05061	0.00383	266	5	262	17
YQ81-34	124	103	0.83	0.04197	0.00067	0.29729	0.01325	0.05137	0.00232	265	4	264	10
YQ81-35	223	206	0.92	0.04100	0.00062	0.29325	0.01179	0.05187	0.00210	259	4	261	9
YQ81-36	55	17	0.31	0.04195	0.00077	0.31005	0.02283	0.05360	0.00399	265	5	274	18
YQ81-37	77	58	0.76	0.04211	0.00073	0.30065	0.02180	0.05178	0.00379	266	5	267	17
YQ81-39	129	105	0.82	0.04163	0.00066	0.29548	0.01465	0.05147	0.00258	263	4	263	11
YQ81-40	133	106	0.80	0.04243	0.00067	0.31463	0.01978	0.05378	0.00340	268	4	278	15
YQ81-41	167	158	0.95	0.04050	0.00063	0.29041	0.01346	0.05200	0.00243	256	4	259	11
YQ81-42	45	20	0.45	0.04111	0.00081	0.28552	0.05593	0.05037	0.00989	260	5	255	44
YQ81-43	128	108	0.85	0.04167	0.00066	0.29561	0.01395	0.05144	0.00245	263	4	263	11
YQ81-44	290	334	1.15	0.04080	0.00061	0.29106	0.01125	0.05173	0.00201	258	4	259	9
YQ89-01	96	68	0.71	0.04075	0.00065	0.28996	0.01582	0.05161	0.00284	33	4	259	12
YQ89-02	153	135	0.88	0.04133	0.00060	0.29282	0.01196	0.05138	0.00211	261	4	261	9
YQ89-03	158	198	1.25	0.04029	0.00060	0.28692	0.01443	0.05164	0.00261	255	4	256	11
YQ89-04	70	43	0.62	0.04014	0.00067	0.28873	0.02078	0.05217	0.00378	254	4	258	16
YQ89-05	75	56	0.75	0.04080	0.00077	0.28745	0.02053	0.05110	0.00370	258	5	257	16
YQ89-06	92	75	0.81	0.04123	0.00066	0.29329	0.01421	0.05159	0.00253	260	4	261	11
YQ89-07	154	134	0.87	0.04044	0.00062	0.29230	0.01215	0.05242	0.00220	256	4	260	10
YQ89-08	79	74	0.94	0.04265	0.00071	0.30072	0.01687	0.05113	0.00290	269	4	267	13
YQ89-09	101	124	1.24	0.04169	0.00065	0.28222	0.01242	0.04909	0.00218	263	4	252	10
YQ89-10	86	72	0.83	0.04121	0.00070	0.29268	0.01854	0.05151	0.00329	260	4	261	15
YQ89-11	112	109	0.97	0.03968	0.00061	0.28116	0.01389	0.05139	0.00256	251	4	252	11
YQ89-12	133	157	1.19	0.04169	0.00063	0.30397	0.01298	0.05288	0.00227	263	4	269	10
YQ89-13	107	88	0.82	0.04228	0.00066	0.29920	0.01478	0.05133	0.00256	267	4	266	12
YQ89-14	120	112	0.94	0.04158	0.00064	0.29572	0.01355	0.05157	0.00238	263	4	263	11
YQ89-15	71	69	0.97	0.04040	0.00075	0.28671	0.01988	0.05147	0.00362	255	5	256	16
YQ89-16	50	25	0.49	0.04174	0.00077	0.29940	0.02315	0.05202	0.00406	264	5	266	18
YQ89-18	277	332	1.20	0.04179	0.00060	0.29723	0.01035	0.05158	0.00180	264	4	264	8
YQ89-19	110	98	0.89	0.04258	0.00068	0.29946	0.01645	0.05100	0.00282	269	4	266	13
YQ89-20	130	102	0.78	0.04169	0.00064	0.29648	0.01480	0.05158	0.00259	263	4	264	12
YQ89-21	156	94	0.60	0.04102	0.00061	0.29012	0.01148	0.05129	0.00204	259	4	259	9
YQ89-22	150	132	0.88	0.04170	0.00064	0.29589	0.01280	0.05145	0.00224	263	4	263	10
YQ89-23	137	120	0.88	0.04067	0.00063	0.28716	0.01239	0.05120	0.00223	257	4	256	10
YQ89-24	159	151	0.95	0.04117	0.00063	0.29021	0.01297	0.05112	0.00230	260	4	259	10
YQ89-25	220	238	1.08	0.04086	0.00060	0.29023	0.01096	0.05151	0.00195	258	4	259	9
YQ89-27	148	134	0.90	0.04272	0.00063	0.30245	0.01298	0.05134	0.00221	270	4	268	10
YQ89-28	122	111	0.91	0.04204	0.00064	0.29958	0.01387	0.05168	0.00241	265	4	266	11
YQ89-30	94	90	0.96	0.04198	0.00067	0.29843	0.01473	0.05155	0.00257	265	4	265	12
YQ89-31	97	77	0.80	0.04149	0.00065	0.29636	0.01567	0.05180	0.00276	262	4	264	12
YQ89-32	88	66	0.75	0.04180	0.00068	0.29623	0.01546	0.05139	0.00271	264	4	263	12
YQ89-34	58	18	0.31	0.04209	0.00074	0.29816	0.01956	0.05137	0.00341	266	5	265	15
YQ89-35	83	81	0.98	0.04170	0.00068	0.29736	0.01812	0.05172	0.00318	263	4	264	14
YQ89-36	58	29	0.50	0.04095	0.00078	0.28665	0.02375	0.05076	0.00425	259	5	256	19
YQ89-37	47	30	0.64	0.04207	0.00086	0.31336	0.04643	0.05402	0.00808	266	5	277	36
YQ89-38	253	264	1.04	0.04198	0.00060	0.30187	0.01175	0.05215	0.00203	265	4	268	9
YQ89-39	107	88	0.82	0.04285	0.00067	0.30212	0.01287	0.05113	0.00220	270	4	268	10
YQ89-40	183	139	0.76	0.04186	0.00062	0.29311	0.01096	0.05078	0.00191	264	4	261	9
YQ89-41	167	210	1.26	0.04140	0.00061	0.29503	0.01168	0.05168	0.00206	262	4	263	9
YQ89-42	210	211	1.01	0.04211	0.00061	0.28727	0.01011	0.04947	0.00175	266	4	256	8
YQ89-43	218	219	1.00	0.04169	0.00061	0.29750	0.01151	0.05175	0.00201	263	4	264	9
YQ89-44	106	114	1.08	0.04212	0.00068	0.31096	0.03124	0.05354	0.00539	266	4	275	24

Notes: The analytical results are reported with a 1σ error. Zircon U–Pb dating with a beam size of 30–40 μm was conducted using LA-ICP-MS at the Key Laboratory of Lithospheric Tectonics and Exploration of the Ministry of Education from the China University of Geosciences (Beijing).

4.1. Geochronology

In this study, three granitic plutons from the Huashigou area were chosen for zircon U–Pb dating. The zircons used were primarily colorless to transparent and euhedral to subeuhedral, with elongated to stubby grains (50–250 μm long with length-to-width ratios of 2:1–4:1). Typical magmatic oscillatory zonation was common, and several inherited cores were observed (see insets in Figure 2). The contents of Th (16–415 × 10⁻⁶) and U (40–440 × 10⁻⁶) were different among these zircons, and the Th/U ratios were consistent with a magmatic origin [45–48]. The detailed analytical results are listed in Table 3. The U–Pb concordia diagrams for Huashigou granitic rocks are shown in Figure 3.



Figure 2. Cathodoluminescence images of zircon grains of granitic rocks from the Huashigou area (ages in Ma).

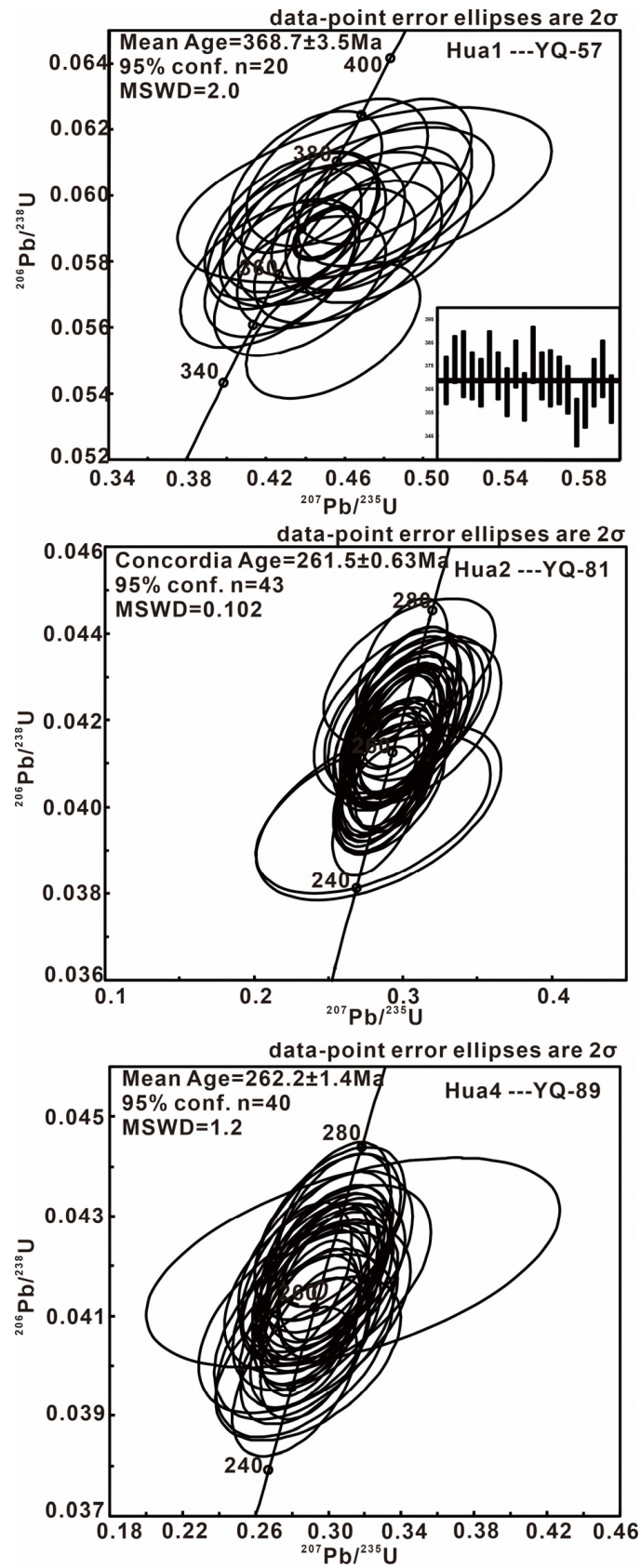


Figure 3. Zircon concordia diagram of granitic rocks. The weighted mean $^{206}\text{Pb}/^{238}\text{U}$ ages for samples YQ-57, YQ-81, and YQ-89 are 368.7 ± 3.5 Ma (MSWD = 2.0; 2σ), 261.5 ± 0.63 Ma (MSWD = 0.102; 2σ), and 262.2 ± 1.4 Ma (MSWD = 1.2; 2σ), respectively.

4.2. Whole-Rock Geochemistry

4.2.1. Hua1 Pluton

Seven samples of granitic rocks (YQ57–YQ63) from the Hua1 pluton were analyzed for major- and trace-element compositions. Loss on ignition (LOI) for all samples was less than 1 wt.%. The granitic samples showed high contents of SiO₂ (67.78–68.48 wt.%) and Al₂O₃ (15.26–15.77 wt.%) but low contents of MgO (1.19–1.38 wt.%) with low Mg[#] (about 38). Their contents of CaO and TiO₂ were 3.39–3.80 wt.% and 0.40–0.48 wt.%, respectively. The Hua1 pluton samples showed total alkali contents ranging from 6.36 to 6.67 wt.% and a slight sodium enrichment (Na₂O/K₂O = 1.16–1.39). They belong to the calc-alkaline series in the SiO₂-K₂O diagram (Figure 4a). Their A/CNK ratios ranged from 0.97 to 0.99, indicating that the Hua1 granites are metaluminous (Figure 4b).

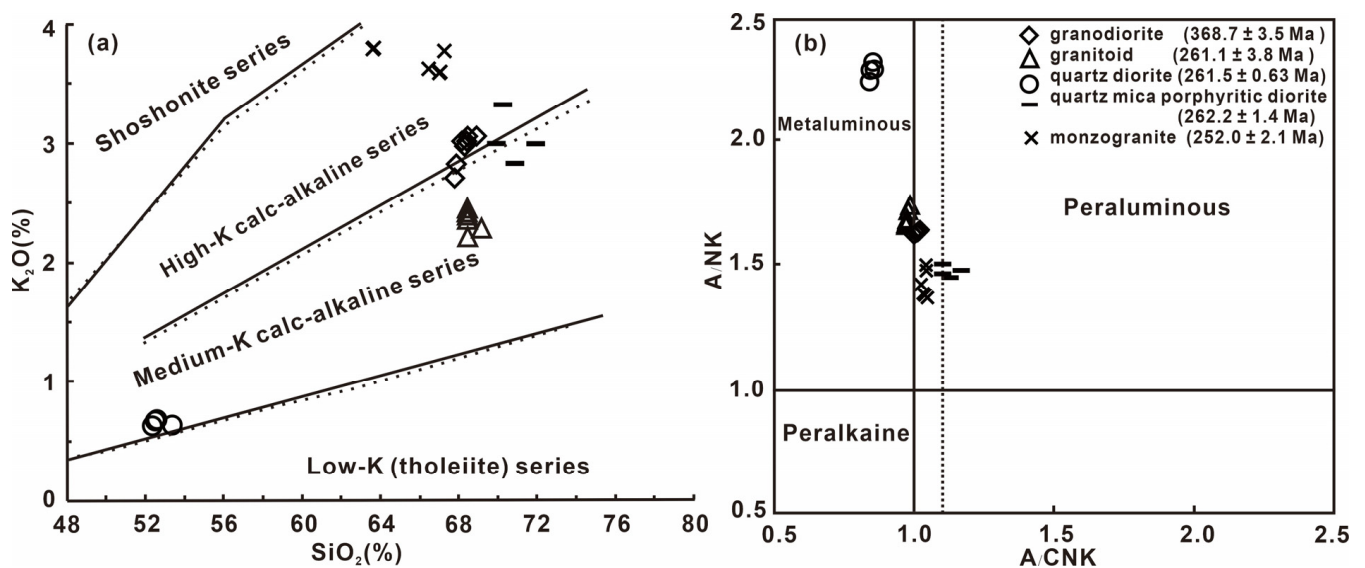


Figure 4. (a) Diagram of SiO₂-K₂O contents; (b) ANK-ACNK diagram of granitic rocks from the Huashigou area. $A/NK = Al_2O_3/Na_2O + K_2O$; $A/CNK = Al_2O_3/CaO + Na_2O + K_2O$.

The Late Devonian granodiorites showed low Sr contents ($205.34\text{--}226.54 \times 10^{-6}$) and high Y contents ($19.41\text{--}23.82 \times 10^{-6}$), with Sr/Y ratios of 9.17–11.67. The Nb/U and Nb/Ta ratios of the Late Devonian granodiorites were 7.77–10.21 and 12.42–14.39, respectively, which are comparable to those of the Earth's crust, i.e., 9–12 [49–52] and 12–13 [53]. The Late Devonian granodiorite samples contained relatively high REE contents ($\Sigma REE = 570\text{--}766 \times 10^{-6}$) and were relatively enriched in light rare-earth elements (LREEs) with moderate LREE/HREE fractionation ($(La/Yb)_N = 12.99\text{--}16.05$ and $(La/Sm)_N = 6.1\text{--}6.91$). Additionally, they showed a flat distribution pattern of heavy rare-earth elements (HREEs) and negative Eu anomalies ($\delta Eu = 0.64\text{--}0.89$). In a primitive-mantle-normalized trace element spider diagram (Figure 5a), the samples showed a notable enrichment in Rb, K, La, Th, and Ce and a relative depletion in Ba, Sr, and Cs. In terms of high-field-strength elements (HFSEs), a notable depletion in Nb, Ta, and Ti and a relative enrichment in Zr and Hf can be observed for these samples.

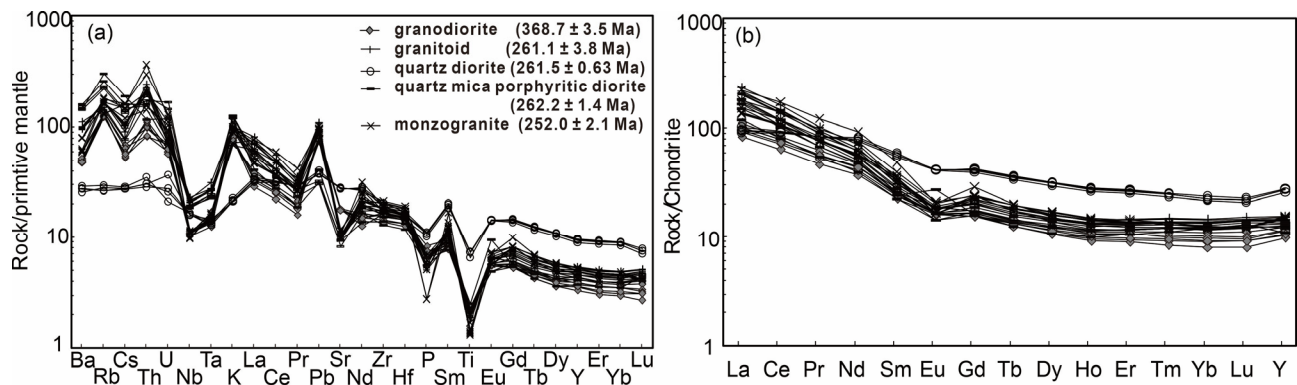


Figure 5. Primitive-mantle-normalized trace element spider diagrams for granitoids (a); chondrite-normalized REE patterns of granitic rocks from the Huashigou area (b) (PM values and chondrite values are derived from [54]).

4.2.2. Hua2 Pluton

The quartz diorites (YQ81–YQ84) from the Hua2 pluton showed relatively low contents of SiO₂ (52.41–53.32 wt.%) and high contents of Al₂O₃ (19.67–19.69 wt.%), TiO₂ (1.4–1.58 wt.%), TFe₂O₃ (8.71–9.23 wt.%), MgO (2.99–3.25 wt.%), and CaO (7.91–8.11 wt.%). Their total alkali contents ranged from 5.38 wt.% to 5.56 wt.%, and the quartz diorites were evidently sodium-enriched and potassium-depleted (Na₂O/K₂O = 7.01–7.55); thus, they were plotted in the calc-alkaline field in a SiO₂–K₂O diagram (Figure 4a). Based on the plot of the A/NK vs. A/CNK diagram, all of the samples are peraluminous (Figure 4b).

As can be seen from the primitive-mantle-normalized diagram (Figure 5a), the quartz diorites were enriched in LILEs, Ba, Rb, Th, and U and depleted in HFSEs, Nb, Ta, and Ti, with high Sr ($573.85\text{--}593.13 \times 10^{-6}$) and Y ($40.1\text{--}43.32 \times 10^{-6}$) contents and a low Sr/Y ratio (13.25–14.79). As shown in the chondrite-normalized distribution pattern (Figure 5b), the quartz diorites were slightly enriched in LREEs ((La/Yb)_N = 3.89–4.76, (La/Sm)_N = 1.54–1.88, and (Gd/Yb)_N = 1.81–1.89), with slightly negative Eu anomalies ($\delta\text{Eu} = 0.81\text{--}0.89$).

4.2.3. Hua4 Pluton

The Middle Permian porphyritic tonalites (YQ89–YQ92) from the Hua4 pluton showed high contents of SiO₂ (63.64–68.51 wt.%), Al₂O₃ (14.89–16.62 wt.%), Mg (MgO = 0.71%–2.5 wt.%, Mg[#] = 45–51), and total alkali (Na₂O + K₂O = 7.3–8.02 wt.%) and low contents of CaO (1.47–2.93 wt.%). In the K₂O vs. SiO₂ diagram (Figure 4a), all of the samples are plotted as part of the calc-alkaline series. Based on the plot of A/NK vs. A/CNK, all of the samples are peraluminous (Figure 4b).

As can be seen in the primitive-mantle-normalized diagram (Figure 5a), the porphyritic tonalites were enriched in Rb, Ba, and Th and relatively depleted in Nb, Ta, and Ti, with low contents of Sr ($172.43\text{--}217.28 \times 10^{-6}$) and Y ($17.05\text{--}20.98 \times 10^{-6}$) and a low Sr/Y ratio (9.22–12.74). As shown in the chondrite-normalized distribution pattern (Figure 5b), the porphyritic tonalites were enriched in LREEs ((La/Yb)_N = 10.34–14.36, (La/Sm)_N = 5.38–6.98, and (Gd/Yb)_N = 1.35–1.47), with negative Eu anomalies ($\delta\text{Eu} = 0.68\text{--}0.76$).

4.3. Whole-Rock Sr–Nd–O and Hf Isotopes

Whole-rock Sr–Nd–O isotope data are presented in Table 2. The Late Devonian granodiorites (YQ57 and YQ63) from the Hua1 pluton showed high values for the initial ⁸⁷Sr/⁸⁶Sr ratio (0.712356 and 0.71195) and low values for the initial ¹⁴³Nd/¹⁴⁴Nd ratio (0.511827 and 0.511815), with negative $\epsilon_{\text{Nd}}(t)$ values of –6.56 and –6.14 and a model age (T_{DM}) of 1.6 Ga. In addition, the sample YQ63 showed an initial ¹⁷⁶Hf/¹⁷⁷Hf ratio value of 0.282484, with an $\epsilon_{\text{Hf}}(t)$ value of –2.06 and a crustal model age of 1.4 Ga.

The Middle Permian granites from the Hua2 pluton showed high I_{Sr} values of 0.705906 and 0.705970 for quartz diorites (YQ83 and YQ84). Porphyritic tonalite (YQ91) showed the highest $(^{87}Sr/^{86}Sr)_{ir}$ value of 0.719527. The quartz diorites (YQ83 and YQ84) showed $\epsilon_{Nd}(t)$ values of +0.78 and +0.82. The porphyritic tonalite (YQ91) from the Hua4 pluton showed the lowest $\epsilon_{Nd}(t)$ value of -8.57 . In addition, the values of $\delta^{18}O_{V-SMOW}$ for quartz diorite (YQ83) from the Hua2 pluton and porphyritic tonalite (YQ91) from the Hua4 pluton were all relatively higher (12.4‰ and 11.8‰, respectively).

5. Discussion

5.1. Petrogenesis

5.1.1. Petrogenesis of the Hua1 Pluton

The Late Devonian granodiorites (YQ57–YQ63) from the Hua1 pluton were rich in Al but poor in Mg, and they were slightly sodium-enriched and potassium-depleted. Additionally, they belong to the metaluminous calc-alkaline series (Figure 6). They showed high contents of Cs, Ba, Rb, Th, and Pb, low contents of Nb, Ta, Sr, and Ti (Figure 5a), high total REEs and LREEs, and a flat HREE pattern (Figure 5b) [34,55,56]. The flat pattern of HREEs implies that there is no garnet residual in the source region. The low Sr and negative Eu anomalies suggest fractional crystallization of plagioclase during magma evolution, indicating that the depth of partial melting is shallow [57]. The negative anomalies of P and Ti, high I_{Sr} values, and negative $\epsilon_{Nd}(t)$ and $\epsilon_{Hf}(t)$ values are potentially the result of the fractional crystallization of apatite and Fe-Ti oxide in the plagioclase-stable region. The $\epsilon_{Nd}(t)$ vs. $\epsilon_{Hf}(t)$ diagram is similar to that of the lower crust (Figure 7). The Sr–Nd–Hf isotopic compositions of granites suggest that they may have been derived from the partial melting of the underplated lower crust.

5.1.2. Petrogenesis of the Hua4 Pluton and Hua2 Pluton

Middle Permian granodiorites resemble the features of the continental crust because of their higher contents of SiO_2 , Al_2O_3 , and K_2O , as well as because they are rich in Ba, Rb, and Th but poor in Nb, Ta, Ti, Sr, etc., and have a higher positive Pb anomaly relative to REEs (Figure 5a), with high I_{Sr} , negative $\epsilon_{Nd}(t)$, and high $\delta^{18}O_{V-SMOW}$ values. The fractional crystallization of plagioclase occurred during the process of rock formation, as evidenced by a slightly negative Eu anomaly (Figure 5b). The negative P and Ti anomalies imply the fractional distillation of apatite and Fe-Ti oxide. In addition, the low Nb/U ratio and Nb content are related to the contamination of materials from the upper crust [53,58]. The high content of Sr and the low contents of Yb and Y in the granodiorites were similar to the contents of those elements [59,60]. However, the isotopic characteristics of low $Mg^\#$ content (≈ 40), high I_{Sr} , low I_{Nd} , and positive $\epsilon_{Nd}(t)$ (+5.51, Sample YQ3) values are clearly different from the isotopic characteristics of typical adakites formed by the partial melting of juvenile subduction slabs [59–64]; however, they are close to the isotopic characteristics of adakites generated by the partial melting of the underplated basaltic lower crust (Figure 5a) [65–67]. Thus, these adakites were formed in crustal environments with thickened slabs at high temperatures after magmas were contaminated by upper crustal materials during magma ascent and certain fractional crystallization of plagioclases [41].

As for Middle Permian granodiorites, the Nb/U and Nb/Ta ratios were slightly higher than those of the continental crust, and the positive $\epsilon_{Nd}(t)$ values indicate that granodiorites originated from the partial melting of the underplated basaltic lower crust with the involvement of mantle materials. The low Nb/U ratio of quartz mica porphyritic diorite also implies magma contamination with upper crustal materials during its ascent. The $\delta^{18}O_{V-SMOW}$ values of quartz diorite and quartz mica porphyritic diorite were significantly higher than the typical mantle values (5.4 ± 0.3 ‰ [68]), indicating that these granitic rocks are derived from the partial melting of the lower crust. With regard to this, we speculate that Middle Permian granitic rocks are the products of post-collisional slab break-off [69].

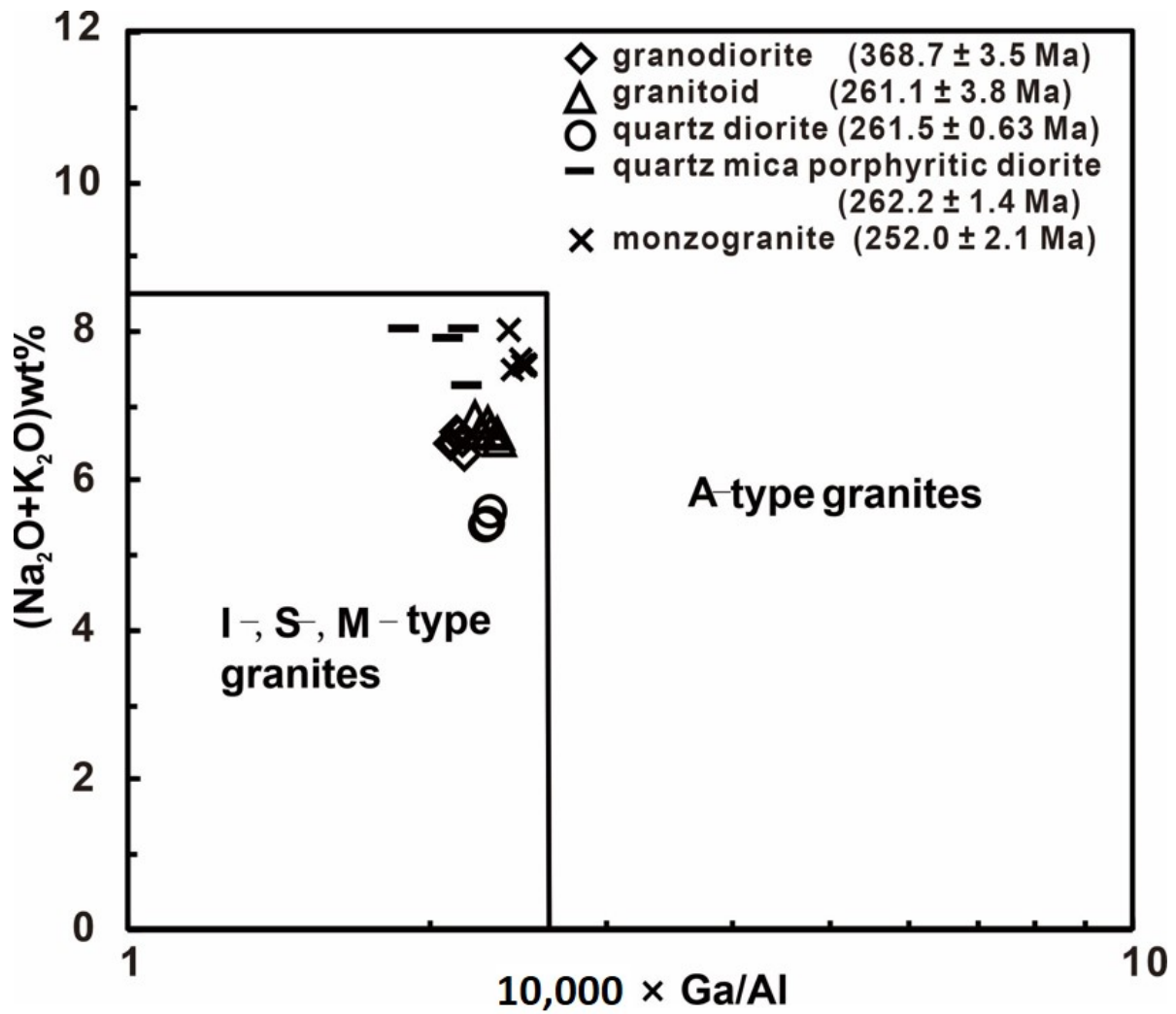


Figure 6. Plot of $10,000 \times \text{Ga/Al}$ vs. $(\text{Na}_2\text{O} + \text{K}_2\text{O})$ in Huashigou granites.

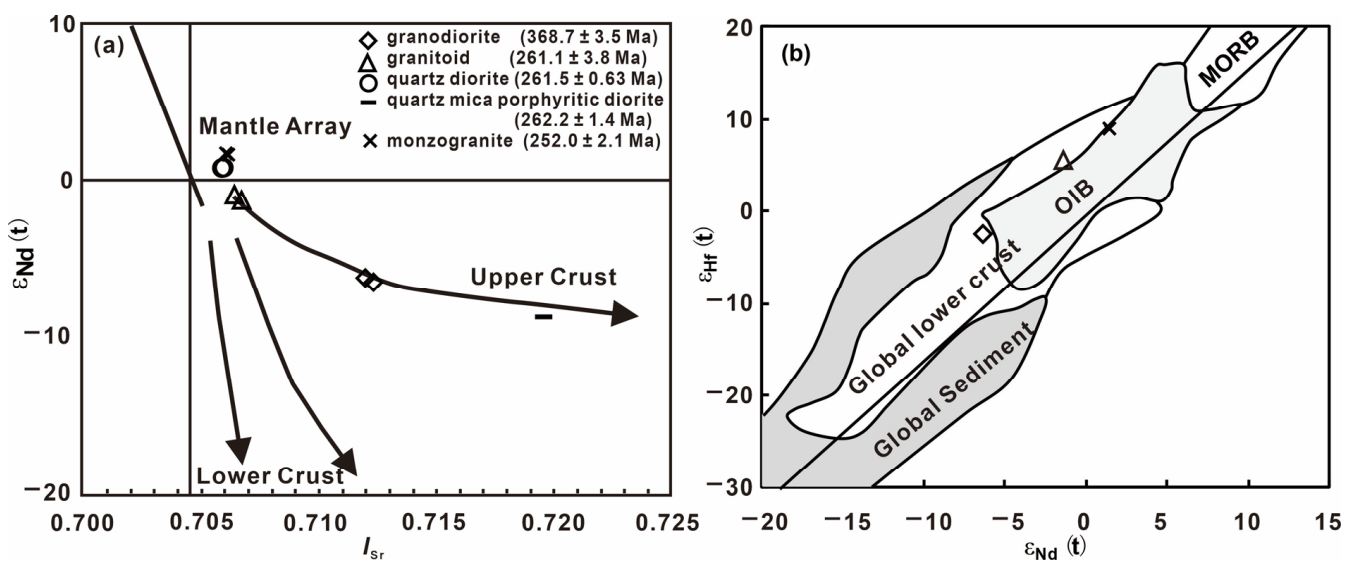


Figure 7. Plots of (a) I_{Sr} vs. $\epsilon_{\text{Hf}}(t)$ and (b) $\epsilon_{\text{Nd}}(t)$ vs. $\epsilon_{\text{Hf}}(t)$ of granites.

The geochemistry characteristics of Middle Permian granitoids are similar to those of Late Permian monzogranites from the Hua5 pluton [42] because of their high contents of Si and Al and low contents of Ti and Mg, as well as Cs, Ba, Rb, Th, and Pb enrichment and Nb, Ta, Sr, and Ti depletion. The Sr–Nd–Hf isotopic compositions showed that monzogranites derived from the partial melting of the underplated Mid-Neoproterozoic basaltic lower crust from the underplating heating of Late Paleozoic basaltic magma [42].

The $\epsilon_{\text{Nd}}(t)$ values of Middle Permian quartz diorite and Late Permian monzogranite were greater than 0 [42], which is similar to some granites formed in environments with extensional tectonics. Granitic rocks with these characteristics have been found only in several areas in the world, such as the New England Batholith [70], northeastern US, southern Quebec of Canada [71,72], the Central Asia–Mongolia fold belt [73–75], etc. These two types of granitic rocks in this area have even lower $\epsilon_{\text{Nd}}(t)$ values. Generally, the characteristic of $\epsilon_{\text{Nd}}(t) < 0$ indicates that a depleted mantle component played an important role in magma formation. In addition, the geochemical characteristics of Middle Permian quartz diorite and Late Permian monzogranite did not show any evidence of crust–mantle mixing in the source region [42]. Comparing this to other granites with $\epsilon_{\text{Nd}}(t) > 0$, granites in this area had lower $\epsilon_{\text{Nd}}(t)$ (closer to 0) values. Therefore, the characteristic of the $\epsilon_{\text{Nd}}(t)$ value, which is slightly greater than 0, may indicate that Middle Permian quartz diorite and Late Permian monzogranite were derived from the partial melting of basic materials in the lower crust formed by underplating.

5.2. Tectonic Setting of Huashigou Granitoids

Wu et al. [76] considered that granite in Phase 4 is related to isostatic adjustments between and among different rock bodies after orogenesis. Leake et al. [77] identified that, during the continental crash with the orogenic belt, the granitic emplacements caused by local temperatures and stresses while intrusions and tensility slumps happened in many ancient orogenic belts in the world were synchronous, e.g., the Sevier orogenic belt in southeast California, USA [78]; Guitiriz granite in the Variscan belt in Northern Spain [79]; and the Proterozoic orogenic belt in South Greenland. Foster et al. [80] showed that rapid exhumation could cause the decompression and partial melting of the lower or upper mantle, leading to the formation of Eocene intrusive rocks. For Late Devonian Huashigou granitoids, the geochemical characteristics indicate that they were formed from the partial melting of the lower crust, and their formation age is the same as that of Phase 4 granitic magma in the North Qaidam, as classified by [76]. In addition, the granites from Tula in the South Altyn Tagh Fault and Yusupuleke Tagh belong to the same period [39,76]. All of them were formed in the background of extensional tectonics after orogenesis. In Haker's diagram (Figure 8), granitic rocks from different eras show favorable correlations, and their contents of Al_2O_3 , MgO, TiO_2 , and TFeO decrease gradually as the SiO_2 content increases, indicating a distinct negative correlation. K_2O and Na_2O show a positive correlation, and Rb, Sr, and Zr increase gradually as SiO_2 contents increase. Additionally, Ba shows a negative correlation (Figure 9). These characteristics showed that the sources of different types of granitic rocks in the Huashigou area are similar. As shown in Figure 10, all samples are plotted in a post-collisional tectonic setting. Combined with the regional tectonic setting, we believe that the rocks were formed during a post-collisional tectonic setting where the previously subducted slab underwent detachment, leading to slab break-off magmatism and the formation of a significant number of granitic rocks.

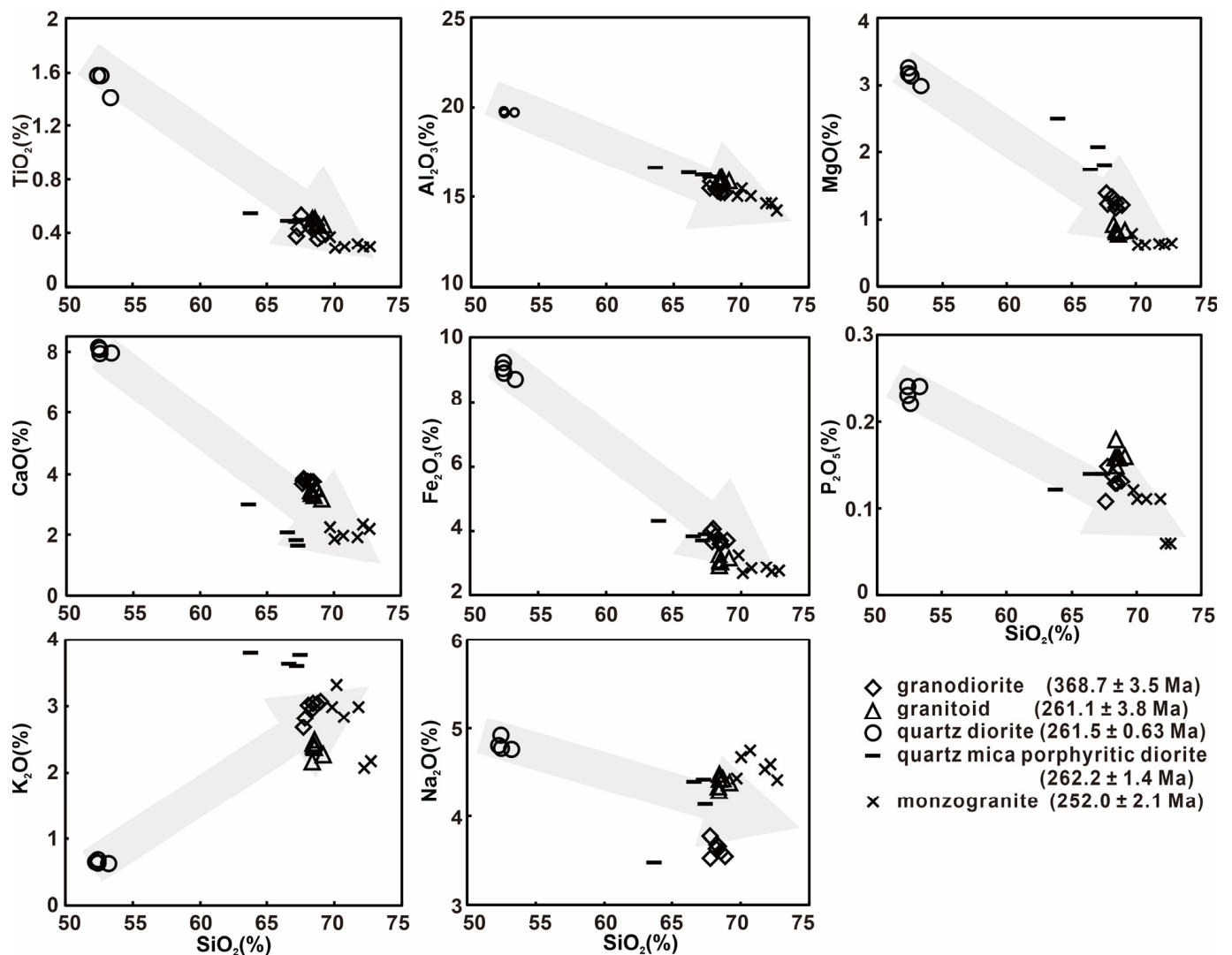


Figure 8. Harker diagrams of Huashiou granitic rocks.

Mid–Late Permian granitoids are comparable to Phase 5 Paleozoic granites in the North Qaidam, as determined by Wu et al. [76], due to the closing of the Paleo-Tethys Ocean, causing the regional tectonic setting to change from tensility to shrinkage. The continental subduction happened before the crust thickened rapidly. In addition, the delamination of the lower crust induced the underplating of basaltic magma, which further elicited the partial melting of the lower crust. Eventually, Mid–Late Permian granitoids were formed. Possessing characteristics of adakites, Mid–Late Permian granodiorites were formed under pressures greater than 1.5 GPa [64,72–87], indicating that the crust thickness could be over 50 km [87,88]. Quartz diorites with high Sr and Yb contents were formed under medium or relatively high pressures, while quartz mica porphyritic diorites with high Sr and Yb contents were formed under medium pressures. The formation depth is estimated to be around 30 km. The depth of the source regions of partial melting decreases gradually from Middle Permian granodiorite to quartz diorite to quartz mica porphyritic diorite. Furthermore, Late Permian monzogranite is similar to granite, with low Sr but high Yb contents. Granite formed under low pressure and potentially at normal crustal thicknesses (≈ 30 km). Therefore, the thickness of the continental crust in the study area might have changed from thick to normal during the Late Permian.

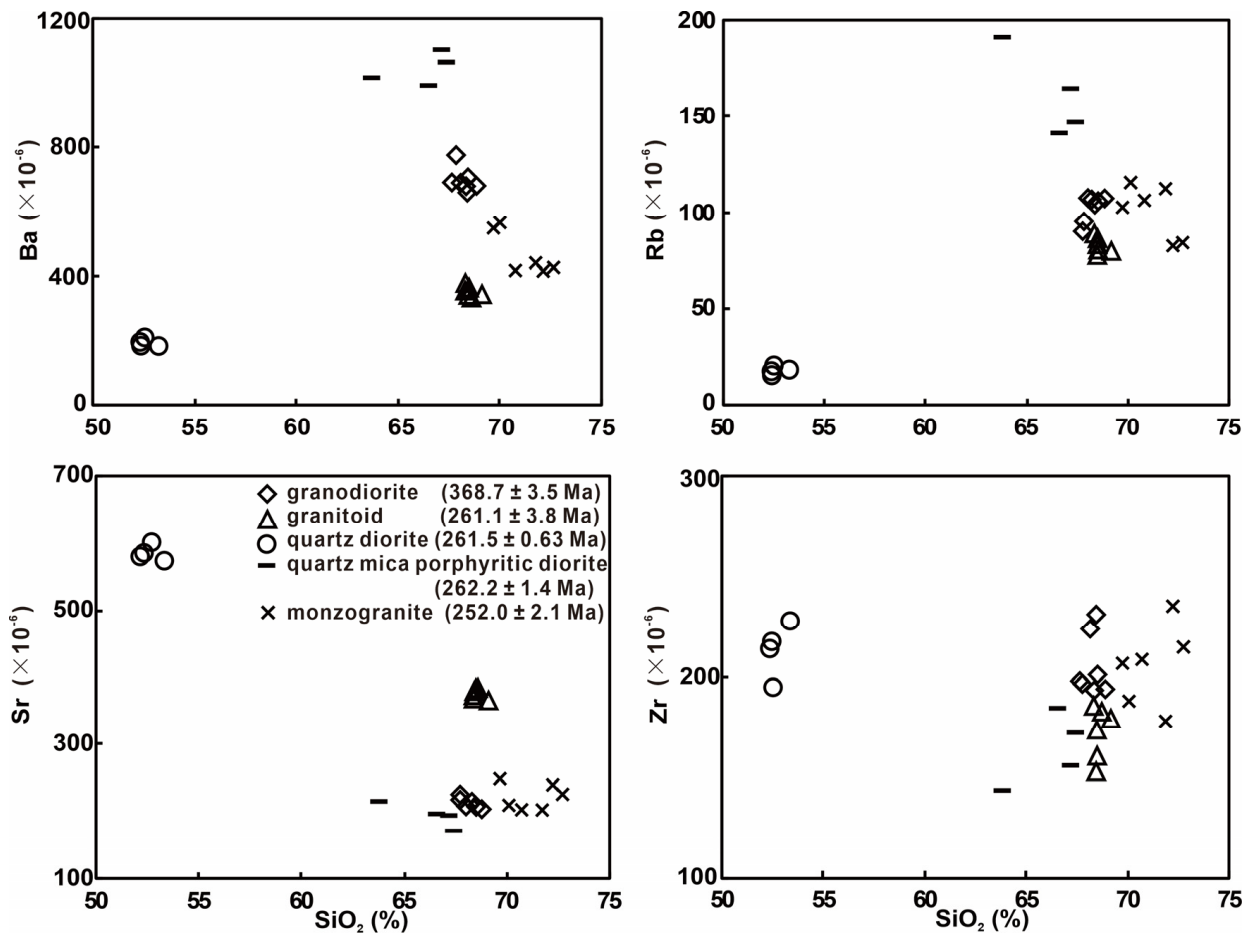


Figure 9. Trace element variation diagrams of granitic rocks from the Huashigou area.

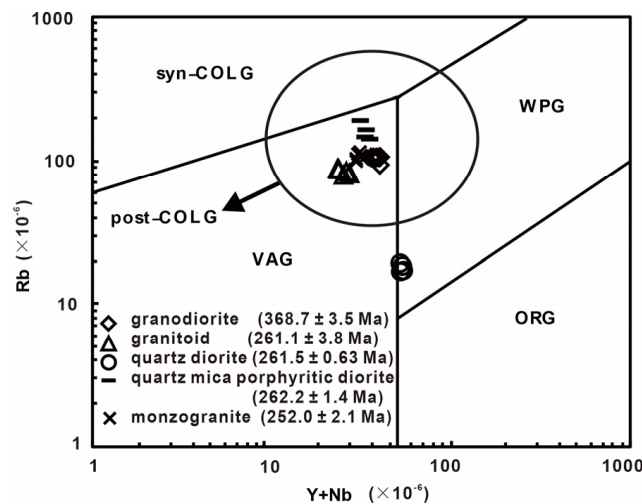


Figure 10. Rb – (Y + Nb) diagram for discriminating the tectonic setting of granitic rocks from the Huashigou area. VAG: volcanic arc granite; ORG: ocean ridge granite; WPG: within-plate granite; syn-COLG: syn-collisional granite; post-COLG: post-collisional granite (after [81]).

It can be concluded that there were at least two important compressional–extensional tectonic transformation phases (c. 369 Ma and c. 262–252 Ma, respectively), with intrusions of granitic magma, which happened in the study area during the period of the Late Paleozoic. Additionally, this demonstrated that the evolution of the Altyn Tagh–Qilian–

North Qaidam tectonic mechanism was evidently divided into phases. The magmatic activities and geochemical characteristics of granites indicate that the crust thickness before c. 369 Ma may have been less than 35 km, with low contents of Sr and high contents of Y. This corresponds to Late Devonian continental lava and volcanic pyroclastic deposits (products of tectonic evolution in the post-orogenic period) developed in the North Qaidam and East Kunlun regions, which are related to extensions of the continental crust [89]. After a short period of extension in the Devonian, the North Margin of the Qinghai–Tibet Plateau was influenced by tectonic movements in the Paleo-Tethys tectonic domain, especially subductions [89]. The ancient Tethys Ocean’s collision transpired between the Carboniferous–Permian continents of Asia and the Gondwana continent as the crust was renewed and intensified the compression. The crust underwent rapid thickening, reaching a thickness of up to 50 km in the Mid–Late Permian (262–252 Ma). Simultaneously, there was a transition phase in the tectonic system from compression to extension, and the basaltic lower crust was partially melted due to the heating of underplated basaltic magma, causing the formation of Mid–Late Permian granites. In conclusion, magmatic activities in the study area in the Early Paleozoic–Devonian were mainly affected by the Altyn Tagh–Qilian–North Qaidam tectonic mechanism, and those of the Carboniferous–Mesozoic–Cenozoic were restricted by the tectonic mechanism of the Paleo-Tethys Plate.

5.3. Tectonic Implications

5.3.1. Tectonic System of Altyn Tagh

Altyn Tagh is an important tectonic belt in the Northern Qinghai–Tibet Plateau, which includes a calc-alkaline granitic body dated at c. 575 Ma [90]. These granodiorites were formed at the active continental margin, meaning that plate subduction happened between the end of the Neoproterozoic and the beginning of the Paleozoic. In the Early Paleozoic, the Altyn Tagh region had started the ocean–continent evolution, as evidenced by two major ophiolite belts of such age. The c. 508–449 Ma Hongliugou–Lapeiquan ophiolite [91,92] is comparable to the Mangnai ophiolite, dated at c. 481 Ma [91]. In recent years, the discovery of high-pressure and ultrahigh-pressure metamorphic rocks in southern Altyn Tagh revealed the existence of a UHP metamorphic belt [7,11,12,28,29,93], formed ca. 504–486 Ma [94], which is 40–60 Ma older than that of eclogite in the UHP metamorphic belt in the North Qaidam Margin. Post-collisional extension was the major tectonic evolution process in the Altyn Tagh region, with weak magmatic activity and small rock masses [89].

5.3.2. North Qaidam–Qilian Tectonic System

North Qaidam–Qilian is a Cambrian–Ordovician orogenic belt. The Southern Qilian region is a small, active ocean basin. The oceanic crust subducted toward the Middle Qilian continental crust, and the ocean basin soon closed and formed the tectonic pattern of today. In recent years, the discovery of eclogites in the Xitie Mountain, Dachaidan, Yuka River, Dulan, and Shaliu River [9,12,95] proved that, during ca. 495–466 Ma, the subducted oceanic crust towed the Qaidam continental crust, causing it to subduct continuously. As a result, different types of rocks in Northern Qaidam experienced Early Paleozoic UHP metamorphism [12,17,18]. Furthermore, coesite and pseudomorph in eclogite and paragneiss [9,12], garnet peridotite, and diamond inclusions, as well as the phenomenon that clinopyroxene and rutile were exsolved in garnet [7], are consistent with these results. Several rocks were subducted to a mantle depth of 100–200 km. In the Early Silurian–Devonian, the continental crust began an exhumation process because of the subducted oceanic crust’s earlier delamination and violent crustal uplift during orogenesis, with magmatic activities in the crust. Molasse formations were broadly developed in the Early Devonian [19,21,96]. Furthermore, quartz diorite of the Aolao River in North Qaidam, small rock bodies southeast of the Bagaqaidam Lake, Datouyangou rock bodies in the Dachaidan region, and Late Devonian granodiorites were formed by the partial melting that occurred during extensions between different blocks in the orogenic zone after the UHP metamorphic belt was subducted and exhumed, indicating the uplifting stage of the North

Qaidam–Qilian region after its orogenesis. This orogenesis stopped in the Carboniferous when the marine-paralic continental deposition belt covered the whole Qilian Caledonides tectonic belt [21]. In the Late Carboniferous, intracontinental subduction happened in North Qaidam as the Paleo-Tethys Ocean closed. Large amounts of granodiorite–monzogranite magmas were created in the middle–lower crust [97], such as the Sanchagou rock body in the west section of North Qaidam [21] and Late Permian monzogranite. These granites were formed under local tectonic stress changes from extension to compression, leading to intracontinental subduction and the upward intrusion of deep-mantle-derived materials. The middle–lower crust was eventually remelted.

5.3.3. Tectonic Setting of Altyn Tagh and North Qaidam–Qilian

Ge et al. [98] considered the tectonic units on both sides of the Altyn Tagh Fault before the Cenozoic Era to be comparable to the Alashan–Beishan–Tarim Block, the North Qilian–Hexi Corridor–Manjiaer Rift Trough, the Middle Qilian Uplift–Middle Uplift of Tarim, the South Qilian–North Qaidam–South Tarim, and the East Kunlun–West Kunlun. Based on a study of eclogites in the North Qaidam and South Altyn Tagh UHP metamorphic belts, Yang et al. [9] concluded that the South Altyn Tagh UHP metamorphic belt was a westward extension of the Northern Qaidam UHP metamorphic belt, with a stagger of 400 km by the Altyn Tagh Fault. Chen et al. [99] considered the east section of Altyn Tagh and the west section of the Qilian Mountain to be similar and comparable, estimating that the total displacement of the sinistral strike-slip of the Altyn Tagh Fault is about 400 km. Research on the metamorphic ages of eclogites has been conducted in Altyn Tagh and North Qaidam. Liu et al. [93] found that the peak metamorphic age of rocks in the Altyn Tagh high-pressure–ultrahigh-pressure metamorphic belt (c. 504–480 Ma) was c. 40–60 Ma earlier than that of Northern Qaidam (c. 461–420 Ma), which is c. 30–55 Ma earlier than the retrograde metamorphic age. Thus, it is considered that eclogites in Altyn Tagh and Northern Qaidam do not belong to the same high-pressure–ultrahigh-pressure metamorphic belts.

Late Paleozoic granites in Northern Qaidam–Qilian can be distinguished in the Late Devonian (c. 385–367 Ma) and Permian (c. 275–252 Ma). However, Late Paleozoic granites are rare in Altyn Tagh. Chen et al. [99] considered that the Early Paleozoic Era (c. 490–385) was the active stage due to magmatic activities in the north margin of Altyn Tagh. Hence, the granite in Altyn Tagh was not found in the study area, which may be caused by the different active ages of the Altyn Tagh and North Qaidam UHP metamorphic belts. Accordingly, the South Altyn Tagh and North Qaidam UHP metamorphic belts may not belong to one UHP metamorphic belt.

5.3.4. Nd Model Age and Attribution of Precambrian Basement in the Qilian Block

The Proterozoic crystalline basements within the Qilian orogenic belt predominantly emerge in the Yemanan Mountains in the western segment, Huangyuan in the central portion, and Maxianshan in the eastern section. These formations comprise high-grade metamorphic and granitic rocks. Generally, there are two models of the tectonic affinity of the Precambrian basement in the Qilian orogenic belt. Researchers consider that the Qilian Block belongs to the North China Craton [100–102]. However, geochemical and isotopic geochronological results led some researchers to consider that the Qilian Block was genetically related to the Yangtze Block. By analyzing the age spectrum of detrital and magmatic zircons in the Qilian Block, we concluded that the Qilian Block and Yangtze Block may have been in a uniform block in the Neoproterozoic Era and both belonged to Gondwana [33,103,104]. Through the study of Precambrian basement rocks in the Qilian orogenic belt and Pb–Nd isotopic compositions of granites, Zhang et al. [88] concluded that the Qilian orogenic belt is similar to the Yangtze Block and expanded the northwest boundary of the Yangtze Block to the north of the Qilian orogenic belt.

Based on the Nd isotope model ages of granites, we concluded that the basement of the North China Plate was formed in the Archean. The most important crustal growth

period was between 2.8 and 2.6 Ga, and the less important crustal growth period was from 1.8 to 2.2 Ga [105]. Simultaneously, through comprehensive data processing and analysis, Wu et al. [106] determined that the Nd isotope model ages of the North China Craton are mainly between 2.4 Ga and 3.6 Ga, and the Nd isotope model ages of the whole South China Craton are mainly between 0.9 Ga and 2.3 Ga, while the intermediate acid igneous rocks in the Yangtze Block are between 0.7 and 2.2 Ga [72]. Furthermore, the Nd model ages of Huashigou granitoids are evidently divided into two phases: 0.9–1.1 Ga, represented by Middle Permian granodiorite, Middle Permian quartz diorite, and Late Permian monzogranite, and 1.6–1.7 Ga, represented by Late Devonian granodiorite and Middle Permian porphyritic tonalite [41,42]. This confirmed that the Mesoproterozoic Era was a crustal growth period in the Qilian region. The results indicate that the crustal growth history of the Qilian orogenic belt is similar to that of the South China Craton but different from that of the North China Craton. Furthermore, the Nd isotope model ages indicated that the Qilian Block and Yangtze Block might have been in a uniform block in the Mesoproterozoic Era.

The results highlighted two stages of granitic production in the Huashigou area, which included Late Devonian granodiorite (c. 369 Ma), Middle Permian biotite granodiorite, quartz diorite, porphyritic tonalite (c. 262–261 Ma), and Late Permian monzonitic granite (252 Ma).

6. Conclusions

- (1) Zircon U–Pb dating yielded crystallization ages of 368.7 ± 3.5 Ma, 261.5 ± 0.63 Ma, and 262.2 ± 1.4 Ma for the Hua1, Hua2, and Hua4 plutons, respectively.
- (2) Trace elements and Sr–Nd–Hf–O isotopes indicated that Huashigou granitoids were derived from the partial melting of the lower crust.
- (3) Huashigou granitoids were formed in the orogenic–post-orogenic extensional tectonic setting, and they were derived from different tectonic levels or crustal depths. Late Devonian granitoids were formed from the decompression melting of enriched and shallow-depth crustal materials. Middle–Late Permian granitoids resulted from the partial melting of the basaltic lower crust through heating by underplating basaltic magma. Additionally, they may have been formed by slab break-off magmatism.

Author Contributions: Y.W.: conceptualization, investigation, visualization, data analysis, writing—original draft, writing—review and editing. W.C.: writing—original draft, writing—review and editing. J.W.: investigation, writing—review and editing. Z.J.: investigation, writing—original draft. Q.T.: writing—original draft, writing—review and editing. P.D.: investigation, writing—review and editing. All authors have read and agreed to the published version of the manuscript.

Funding: This study was funded by the projects of the Science and Technology Program of Gansu Province (22YF7GA050), the Gansu Province Youth Talent Project (2020RCXM152), the Central Government Guides Local Funds for Scientific and Technological Development (YDZX20216200001297), the Second Comprehensive Scientific Expedition to the Qinghai–Tibet Plateau (2019QZKK0704), PhD Research Startup Foundation of Hunan University of Arts and Science (No.23BSQD05, No.23BSQD07, and No.21BSQD32), the National Key Research and Development Program of China (2023YFC2908700), the National Natural Science Foundation of China (U2244204), Key Talent Projects in the Gansu Province (2023), and Gansu Province Key Research and Development Program—Industrial Projects (23YFGA0001).

Data Availability Statement: The original contributions presented in the study are included in the article.

Acknowledgments: We appreciate three anonymous reviewers for their constructive suggestions, which greatly improved the manuscript.

Conflicts of Interest: This manuscript has not been published elsewhere and is not under consideration by another journal. The authors have approved the manuscript and agree with its submission to *Minerals*. There are no conflicts of interest to declare.

References

1. Yin, H.F.; Zhang, K.X. Evolution and characteristics of the Central Orogenic Belt. *Earth Sci.-J. China Univ. Geosci.* **1998**, *23*, 437–442. (In Chinese with English abstract)
2. Lu, S.N.; Yu, H.F.; Li, H.K.; Chen, Z.H.; Wang, H.C.; Zhang, C.L.; Xiang, Z.Q. Early Paleozoic suture zones and tectonic divisions in the “Central China Orogen”. *Geol. Bull. China* **2006**, *25*, 1368–1380. (In Chinese with English abstract)
3. Xu, Z.Q.; Yang, J.S.; Li, H.B.; Yao, J.X. The early Paleozoic terrane framework and the formation of the high-pressure (HP) and ultra-high pressure (UHP) metamorphic belts at the Central Orogenic Belt (COB). *Acta Geol. Sin.* **2006**, *80*, 1793–1806. (In Chinese with English abstract)
4. Qiu, H.N.; Wijbrans, J.R. The Paleozoic metamorphic history of the Central orogenic belt of China from $^{40}\text{Ar}/^{39}\text{Ar}$ geochronology of eclogite garnet fluid inclusions. *Earth Planet. Sci. Lett.* **2008**, *268*, 501–514. [[CrossRef](#)]
5. Yang, J.S.; Xu, Z.Q.; Ma, C.Q.; Wu, C.L.; Zhang, J.X.; Wang, Z.Q.; Wang, G.C.; Zhang, H.F.; Dong, Y.P.; Lai, S.C. Compound orogeny and scientific problems concerning the Central Orogenic Belt of China. *Geol. China* **2010**, *37*, 1–11. (In Chinese with English abstract)
6. Liu, L.; Che, Z.C.; Luo, J.H.; Wang, Y.; Gao, Z.J. Recognition and implication of eclogite in the western Altun Mountains, Xinjiang. *Chin. Sci. Bull.* **1997**, *42*, 931–934. (In Chinese with English abstract) [[CrossRef](#)]
7. Liu, L.; Chen, D.L.; Zhang, A.D.; Sun, Y.; Wang, Y.; Yang, J.Q.; Luo, J.H. Ultrahigh pressure gneissic K-feldspar garnet clinopyroxene in the Altyn Tagh, NW China: Evidence from clinopyroxene exsolution in garnet. *Sci. China (D)* **2005**, *48*, 1000–1010. (In Chinese with English abstract) [[CrossRef](#)]
8. Sobel, E.R.; Arnaud, N.; Jolivet, M.; Ritts, B.D.; Brunei, M. Jurassic to Cenozoic exhumation history of the Altyn Tagh range, northwest China, constrained by $^{40}\text{Ar}/^{39}\text{Ar}$ and apatite fission track thermochronology. *Paleoz. Mesoz. Tecton. Evol. Cent. East. Asia* **2001**, *194*, 247–267.
9. Yang, J.S.; Xu, Z.Q.; Zhang, J.X.; Chu, C.Y.; Zhang, R.Y.; Liou, J.G. Tectonic significance of early Paleozoic high-pressure rocks in Altun-Qaidam-Qilian mountains, northwest China. *Mem.-Geol. Soc. Am.* **2001**, *194*, 151–170.
10. Yang, J.S.; Wu, C.L.; Zhang, J.X.; Shi, R.D.; Meng, F.C.; Wooden, J.; Yang, H.Y. Protolith of eclogites in the north Qaidam and Altun UHP terrane, NW China: Earlier oceanic crust? *J. Asian Earth Sci.* **2006**, *28*, 185–204. [[CrossRef](#)]
11. Zhang, J.X.; Zhang, Z.M.; Xu, Z.Q.; Yang, J.S.; Cui, J.W. Petrology and geochronology of eclogites from the western segment of the Altyn Tagh, northwestern China. *Lithos* **2001**, *56*, 187–206. [[CrossRef](#)]
12. Zhang, J.X.; Yang, J.S.; Xu, Z.Q.; Meng, F.C.; Li, H.B.; Shi, R.D. Evidence for UHP metamorphism of eclogites from the Altun Mountains. *Chin. Sci. Bull.* **2002**, *47*, 751–755. (In Chinese with English abstract) [[CrossRef](#)]
13. Zhang, J.X.; Mattinson, C.G.; Meng, F.C.; Wan, Y.S. An early palaeozoic HP/HT granulite-garnet peridotite association in the south altyn tagh, nw china: P-T history and U-Pb geochronology. *J. Metamorph. Geol.* **2005**, *23*, 491–510. [[CrossRef](#)]
14. Zhang, J.X.; Yang, J.S.; Mattinson, C.G.; Xu, Z.Q.; Meng, F.C.; Shi, R.D. Two contrasting eclogite cooling histories, North Qaidam HP/UHP terrane, western China: Petrological and isotopic constraints. *Lithos* **2005**, *84*, 51–76. [[CrossRef](#)]
15. Zhang, J.X.; Meng, F.C.; Li, J.P.; Mattinson, C.G. Coesite in eclogite from the North Qaidam Mountains and its implications. *Chin. Sci. Bull.* **2009**, *54*, 1105–1110. (In Chinese with English abstract) [[CrossRef](#)]
16. Wan, Y.S.; Xu, Z.Q.; Yang, J.S.; Zhang, J.X. The Precambrian High-grade basement of the Qilian Terrane and Neighboring areas: Its ages and compositions. *Acta Geosci. Sin.* **2003**, *24*, 319–324. (In Chinese with English abstract)
17. Song, S.G.; Niu, Y.L. Ultra-deep origin of garnet peridotite from the North Qaidam ultrahigh-pressure belt, Northern Tibetan Plateau, NW China. *Am. Mineral.* **2004**, *89*, 1330–1336. [[CrossRef](#)]
18. Song, S.G.; Zhang, L.; Niu, Y.L.; Su, L.; Jian, P.; Liu, D. Geochronology of diamond-bearing zircons from garnet peridotite in the North Qaidam UHPM belt, Northern Tibetan Plateau: A record of complex histories from oceanic lithosphere subduction to continental collision. *Earth Planet. Sci. Lett.* **2005**, *234*, 99–118. [[CrossRef](#)]
19. Song, S.G.; Zhang, L.; Niu, Y.L.; Su, L.; Song, B.; Liu, D. Evolution from oceanic subduction to continental collision: A case study from the Northern Tibetan Plateau based on geochemical and geochronological data. *J. Petrol.* **2006**, *47*, 435–455. [[CrossRef](#)]
20. Song, S.G.; Su, L.; Li, X.H.; Niu, Y.L.; Zhang, L. Grenville-age orogenesis in the Qaidam-Qilian block: The link between South China and Tarim. *Precambrian Res.* **2012**, *220*, 9–22. [[CrossRef](#)]
21. Song, S.G.; Niu, Y.L.; Su, L. Tectonics of the North Qilian orogen, NW China. *Gondwana Res.* **2013**, *23*, 1378–1401. [[CrossRef](#)]
22. Yang, S.; Li, Z.; Chen, H.; Santosh, M.; Dong, C.; Yu, X. Permian bimodal dyke of Tarim Basin, NW China: Geochemical characteristics and tectonic implications. *Gondwana Res.* **2007**, *12*, 113–120. [[CrossRef](#)]
23. Xiao, W.J.; Windley, B.F.; Yong, Y.; Yan, Z.; Yuan, C.; Liu, C.Z.; Li, J.L. Early Paleozoic to Devonian multiple-accretionary model for the Qilian Shan, NW China. *J. Asian Earth Sci.* **2009**, *35*, 323–333. [[CrossRef](#)]
24. Dong, S.L.; Li, Z.; Gao, J.; Zhu, L. Progress of studies on early Paleozoic tectonic framework and crystalline rock geochronology in Altun-Qilian-Kunlun Orogen. *Geol. Rev.* **2013**, *59*, 731–746.
25. Wang, C.; Liu, L.; Yang, W.Q.; Zhu, X.H.; Cao, Y.T.; Kang, L.; Chen, S.F.; Li, R.S.; He, S.P. Provenance and ages of the altyn complex in altyn tagh: Implications for the early neoproterozoic evolution of northwestern china. *Precambrian Res.* **2013**, *230*, 193–208. [[CrossRef](#)]
26. Yu, S.Y.; Zhang, J.X.; del Real, P.G.; Zhao, X.L.; Hou, K.J.; Gong, J.H.; Li, Y.S. The Grenvillian orogeny in the Altun-Qilian-North Qaidam mountain belts of northern Tibet Plateau: Constraints from geochemical and zircon U-Pb age and Hf isotopic study of magmatic rocks. *J. Asian Earth Sci.* **2013**, *73*, 372–395. [[CrossRef](#)]

27. Zhang, G.; Zhang, L.; Christy, A.G. From oceanic subduction to continental collision: An overview of HP–UHP metamorphic rocks in the North Qaidam UHP belt, NW China. *J. Asian Earth Sci.* **2013**, *63*, 98–111. [[CrossRef](#)]
28. Liu, L.; Sun, Y.; Xiao, P.X.; Che, Z.C.; Luo, J.H.; Chen, D.L.; Wang, Y. Discovery of ultrahighpressure magnesite-bearing garnet lherzolite (>3.8 GPa) in the Altyn Tagh, Northwest China. *Chin. Sci. Bull.* **2002**, *47*, 881–886. (In Chinese with English abstract) [[CrossRef](#)]
29. Liu, L.; Sun, Y.; Luo, J.H.; Wang, Y.; Chen, D.L.; Zhang, A.D. Ultra-high pressure metamorphism of granitic gneiss in the Yinggelisayi area, Altun Mountains, NW China. *Sci. China (D)* **2004**, *47*, 338–346. (In Chinese with English abstract) [[CrossRef](#)]
30. Zhang, A.D.; Liu, L.; Sun, Y.; Chen, D.L.; Wang, Y.; Luo, J.H. SHRIMP U-Pb zircon ages for the UHP metamorphosed granitoid gneiss in Altyn Tagh and their geological significance. *Chin. Sci. Bull.* **2004**, *49*, 2527–2532. (In Chinese with English abstract) [[CrossRef](#)]
31. Yu, S.Y.; Zhang, J.X.; Gong, J.H. Zr-in-rutile thermometry in HP/HP granulite in the Bashiwake area of the South Altun and its geological implications. *Earth Sci. Front.* **2011**, *18*, 140–150. (In Chinese with English abstract)
32. Li, Y.S.; Zhang, J.X.; Li, S.R.; Yu, S.Y.; Gong, J.H.; Lin, Y.H. Metamorphic evolution of the Bashiwake garnet peridotite from the South Altyn Tagh. *Acta Petrol. Sin.* **2013**, *29*, 2073–2092. (In Chinese with English abstract)
33. Xu, W.C.; Zhang, H.F.; Liu, X.M. U-Pb zircon dating constraints on formation time of Qilian high-grade metamorphic rock and its tectonic implication. *Sci. Bull.* **2007**, *52*, 531–538. (In Chinese with English abstract) [[CrossRef](#)]
34. Barbarin, B. A review of the relationships between granitoid types, their origins and their geodynamic environments. *Lithos* **1999**, *46*, 605–626. [[CrossRef](#)]
35. Qi, X.X.; Li, H.B.; Wu, C.L.; Yang, J.S.; Zhang, J.X.; Meng, F.C.; Shi, R.D.; Chen, S.Y. SHRIMP U-Pb zircon dating for Qiashikansayi granodiorite, the Northern Altyn Tagh Mountains and its geological implications. *Sci. Bull.* **2005**, *50*, 440–445. (In Chinese with English abstract) [[CrossRef](#)]
36. Qi, X.X.; Wu, C.L.; Li, H.B. SHRIMP U-Pb age of zircons from Kazisayi granite in the northern Alty Tagh mountains and its significations. *Acta Petrol. Sin.* **2005**, *21*, 859–866. (In Chinese with English abstract)
37. Wang, J.R.; Guo, Y.S.; Fu, S.M.; Chen, J.L.; Qin, X.F.; Zhang, H.P.; Yang, Y.J. Early Paleozoic adakitic rocks in Heishishan, Gansu and their significance for tectonodynamics. *Acta Petrol. Sin.* **2005**, *21*, 977–985. (In Chinese with English abstract)
38. Kusky, T.; Li, J.H.; Santosh, M. The Paleoproterozoic North Hebei Orogen: North China’s collisional suture with the Columbia supercontinent. *Gondwana Res.* **2007**, *12*, 4–28. [[CrossRef](#)]
39. Wang, C.; Liu, L.; Zhang, A.D.; Yang, W.Q.; Cao, Y.T. Geochemistry and petrography of early Paleozoic Yusupuleke Tagh rapakivi-textured granite complex, South Altyn: An example for magma mixing. *Acta Petrol. Sin.* **2008**, *24*, 2809–2819. (In Chinese with English abstract)
40. Xiao, W.J.; Windley, B.F.; Allen, M.B. Paleozoic multiple accretionary and collisional tectonics of the Chinese Tianshan orogenic collage. *Gondwana Res.* **2013**, *23*, 1316–1341. [[CrossRef](#)]
41. Jia, Z.L.; Chen, W.F.; Sha, X.; Wang, J.R. Discovery of middle Permian adakitic rocks in south Qilian area, Gansu and implications for tectonics and Cu(Au) mineralization. *Geotecton. Metallog.* **2017**, *156*, 222–234. (In Chinese with English abstract)
42. Hu, W.L.; Jia, Z.L.; Wang, J.R.; Hou, K.X.; Wang, S.H. Geochronology and geochemistry characteristics of the granites from the Huashigou area, south Qilian and their tectonic significance. *Geol. J. China Univ.* **2016**, *22*, 242–253. (In Chinese with English abstract)
43. Ralf, L. How Does Water Bind to Metal Surfaces: Hydrogen Atoms Up or Hydrogen Atoms Down? *Angew. Chem. Int. Ed.* **2003**, *42*, 3458–3460.
44. Andersen, T. Correction of common lead in U-Pb analyses that do not report ²⁰⁴Pb. *Chem. Geol.* **2002**, *193*, 59–79. [[CrossRef](#)]
45. Vavra, G. On The Kinematics of Zircon Growth and Its Petrogenetic Significance: A Cathodoluminescence Study. *Contrib. Mineral. Petrol.* **1990**, *106*, 90–99. [[CrossRef](#)]
46. Paterson, B.A.; Stephens, W.E.; Rogers, G.; Williams, I.S.; Hinton, R.W.; Herd, D.A. The Nature of Zircon Inheritance In Two Granite Plutons. *Earth Sci.* **1992**, *83*, 459–471.
47. Rubatto, D.; Gebauer, D. *Use of Cathodoluminescence for U-Pb Zircon Dating by Ion Microprobe: Some Examples From The Western Alps. Cathodoluminescence In Geosciences*; Springer: Berlin/Heidelberg, Germany, 2000; pp. 373–400.
48. Möller, A.; O’Brien, P.J.; Kennedy, A.; Kroner, A. Linking Growth Episodes of Zircon and Metamorphic Textures To Zircon Chemistry: An Example From The Ultrahigh-Temperature Granulites of Rogaland (Sw Norway). *Geol. Soc. Lond. Spec. Publ.* **2003**, *220*, 65–81. [[CrossRef](#)]
49. Taylor, S.R.; McLennan, S.M.; Armstrong, R.L.; Tarney, J. The composition and evolution of the continental crust: Rare earth element evidence from sedimentary rocks [and discussion]. *Philosophical Transactions of the Royal Society of London. Ser. A Math. Phys. Sci.* **1981**, *301*, 381–399.
50. Taylor, S.R.; McLennan, S.M. *The Continental Crust: Its Composition and Evolution*; Blackwell: London, UK, 1985; pp. 57–72.
51. Wedepohl, K.H. Der primäre Erdmantel und die durch Krustenbildung verarmte Mantelzusammensetzung. *Fortschr. Min.* **1981**, *59*, 203–205.
52. Weaver, B.L.; Tarney, J. Empirical approach to estimating the composition of the continental crust. *Nature* **1984**, *310*, 575–577. [[CrossRef](#)]
53. Barth, M.G.; McDonough, W.F.; Rudnick, R.L. Tracking the budget of Nb and Ta in the continental crust. *Chem. Geol.* **2000**, *165*, 197–213. [[CrossRef](#)]

54. Sun, S.S.; McDonough, W.F. Chemical and Isotopic Systematics of Oceanic Basalts: Implications for Mantle Composition and Processes. In *Magma In The Ocean Basins*; Saunders, A.D., Norry, M.J., Eds.; Geological Society Special Publications: London, UK, 1989; Volume 42, pp. 313–345.
55. Condie, K.C. Mafic crustal xenoliths and the origin of the lower continental crust. *Lithos* **1999**, *46*, 95–101. [[CrossRef](#)]
56. Davies, G.R.; Macdonald, R. Crustal influences in the petrogenesis of the Naivasha basalt-comendite complex: Combined trace element and Sr-Nd-Pb isotope constraints. *J. Pet.* **1987**, *28*, 1009–1031. [[CrossRef](#)]
57. Whalen, J.B.; Currie, K.L.; Chappell, B.W. A-type granites: Geochemical characteristics, discrimination and petrogenesis. *Contrib. Mineral. Petrol.* **1987**, *95*, 407–419. [[CrossRef](#)]
58. Hofmann, A.W.; Jochum, K.P.; Seufert, M.; White, W.M. Nb and Pb in oceanic basalts: New constraints on mantle evolution. *Earth Planet. Sci. Lett.* **1986**, *79*, 33–45. [[CrossRef](#)]
59. Defant, M.J.; Drummond, M.S. Derivation of some modern arc magmas by melting of young subducted lithosphere. *Nature* **1990**, *347*, 662–665. [[CrossRef](#)]
60. Defant, M.J. Reply for comment by R. Conner on the “Evidence suggests slab melting in arc magmas” by M. Defant and P. Kepezhinskis (EOS, 2001, 82:65, 68–69). *Eos Trans. Am. Geophys. Union* **2002**, *66*, 256–257. [[CrossRef](#)]
61. Kay, S.M.; Ramos, V.A.; Marquez, M. Evidence in Cerro Pampa volcanic rocks of slab melting prior to ridge trench collision in southern South America. *J. Geol.* **1993**, *101*, 703–714. [[CrossRef](#)]
62. Yogodzinski, G.M.; Kay, R.W.; Volynets, O.N.; Koloskov, A.V.; Kay, S.M. Magnesian andesite in the western Aleutian Komandorsky region: Implications for slab melting and processes in the mantle wedge. *Geol. Soc. Am.* **1995**, *107*, 505–519. [[CrossRef](#)]
63. Stern, C.R.; Kilian, R. Role of the subducted slab, mantle wedge and continental crust in the generation of adakites from the Austral volcanic zone. *Contrib. Min. Pet.* **1996**, *123*, 263–281. [[CrossRef](#)]
64. Rapp, R.P.; Shimizu, N.; Norman, M.D.; Applegate, G.S. Reaction between slab-derived melts and peridotite in the mantle wedge: Experimental constraints at 3.8 GPa. *Chem. Geol.* **1999**, *160*, 335–356. [[CrossRef](#)]
65. Peacock, S.M.; Rushmer, T.; Thompson, A.B. Partial melting of subducting oceanic crust. *Earth Planet. Sci. Lett.* **1994**, *121*, 227–244. [[CrossRef](#)]
66. Muir, R.J.; Weaver, S.D.; Bradshaw, J.D.; Eby, G.N.; Evans, J.A. The Cretaceous Separation Point batholith, New Zealand: Granitoid magmas formed by melting of mafic lithosphere. *J. Geol. Soc.* **1995**, *152*, 689–701. [[CrossRef](#)]
67. Petford, N.; Atherton, M. Na-rich partial melts from newly underplated basaltic crust: The Cordillera Blanca Batholith, Peru. *J. Petrol.* **1996**, *37*, 1491–1521. [[CrossRef](#)]
68. Kemp, A.I.S.; Hawkesworth, C.J.; Foster, G.L.; Paterson, B.A.; Woodhead, J.D.; Hergt, J.M.; Whitehouse, M.J. Magmatic and crustal differentiation history of granitic rocks from Hf-O isotopes in zircon. *Science* **2007**, *315*, 980–983. [[CrossRef](#)] [[PubMed](#)]
69. Whalen, J.B.; Hildebrand, R.S. Trace element discrimination of arc, slab failure, and A-type granitic rocks. *Lithos* **2019**, *348–349*, 105179. [[CrossRef](#)]
70. DePaolo, D.J. Age dependence of the composition of continental crust: Evidence from Nd isotopic variations in granitic rocks. *Earth Planet. Sci. Lett.* **1988**, *90*, 263–271. [[CrossRef](#)]
71. Landoll, J.D.; Foland, K.A. The formation of quartz syenite by crustal contamination at Mont Shefford and other Montere-gian complexes, Quebec. *Can. Mineral.* **1996**, *34*, 301–324.
72. Chen, J.F.; Jahn, B.M. Crustal evolution of southeastern China: Nd and Sr isotopic evidence. *Tectonophysics* **1998**, *284*, 101–133. [[CrossRef](#)]
73. Zhao, Z.H.; Wang, Z.G.; Zou, T.R.; Masuda, A. The REE, isotopic composition of O, Pb, Sr and Nd and diagenetic model of granitoids in Altay region. In *New Improve-Ment of Solid Geosciences in Northern Xinjiang*; Tu, G.Z., Ed.; Science Press: Beijing, China, 1993; pp. 239–266. (In Chinese)
74. Zhao, Z.H.; Wang, Z.G.; Zou, T.R.; Masuda, A. Study on petrogenesis of alkali-rich intrusive rocks of Ulungur, Xinjiang. *Geochimica* **1996**, *25*, 205–220. (In Chinese with English abstract)
75. Chen, J.F.; Zhou, T.X.; Xie, Z.; Zhang, X.; Guo, X.S. Formation of positive $\epsilon\text{Nd}(T)$ granitoids from the Alataw Mountains, Xinjiang, China, by mixing and fractional crystallization: Implication for Phanerozoic crustal growth. *Tectonophysics* **2000**, *328*, 53–67. [[CrossRef](#)]
76. Wu, S.P.; Wu, C.L.; Wang, M.Y.; Chen, Q.L.; Wooden, J.L. SHRIMP U-Pb zircon dating of the Tula granite pluton on the south side of the Altun Fault and its geological implications. *Acta Geol. Sin.-Engl. Ed.* **2008**, *82*, 409–414.
77. Leake, B.E. Granite magmas: Their sources, initiation and consequences of emplacement. *J. Geol. Soc.* **1990**, *147*, 579–589. [[CrossRef](#)]
78. Kula, J.L.; Spell, T.L.; Wells, M.L. Syntectonic Intrusion and Exhumation of a Mesozoic Plutonic Complex in the Late Cretaceous, Granite Mountains, Southeastern California. 2002. Available online: https://www.researchgate.net/publication/313524963_Syntectonic_intrusion_and_exhumation_of_a_Mesozoic_plutonic_complex_in_the_Late_Cretaceous_Granite_Mountains_southeastern_California (accessed on 31 January 2002).
79. Aranguren, A.; Tubia, J.; Bouchez, J.L.; Vigneresse, J.L. The Guitiriz granite, Variscan belt of northern Spain: Extension-controlled emplacement of magma during tectonic escape. *Earth Planet. Sci. Lett.* **1996**, *139*, 165–176. [[CrossRef](#)]
80. Foster, D.A.; Schafer, C.; Fanning, C.M.; Hyndman, D.W. Relationships between crustal partial melting, plutonism, orogeny, and exhumation: Idaho-Bitterroot batholith. *Tectonophysics* **2001**, *342*, 313–350. [[CrossRef](#)]

81. Pearce, J.A.; Harris, N.B.W.; Tindle, A.G. Trace element discrimination diagrams for the tectonic interpretation of granitic rocks. *J. Petrol.* **1984**, *25*, 956–983. [[CrossRef](#)]
82. Hellman, P.L.; Green, T.H. The role of sphene as an accessory phase in the high-pressure partial melting of hydrous mafic compositions. *Earth Planet. Sci. Lett.* **1979**, *42*, 191–201. [[CrossRef](#)]
83. Sen, C.; Dunn, T. Dehydration melting of a basaltic composition amphibolite at 1.5 and 2.0 GPa: Implications for the origin of adakites. *Contrib. Mineral. Petrol.* **1994**, *117*, 394–409. [[CrossRef](#)]
84. Liu, J.; Bohlen, S.R.; Ernst, W.G. Stability of hydrous phases in subducting oceanic crust. *Earth Planet. Sci. Lett.* **1996**, *143*, 161–171. [[CrossRef](#)]
85. Klemme, S.; Blundy, J.D.; Wood, B.J. Experimental constraints on major and trace element partitioning during partial melting of eclogite. *Geochim. Et Cosmochim. Acta* **2002**, *66*, 3109–3123. [[CrossRef](#)]
86. Xiao, L.; Clemens, J.D. Origin of potassic (C-type) adakite magmas: Experimental and field constraints. *Lithos* **2007**, *95*, 399–414. [[CrossRef](#)]
87. Xiong, X.L.; Adam, J.; Green, T.H. Rutile stability and rutile/melt HFSE partitioning during partial melting of hydrous basalt: Implications for TTG genesis. *Chem. Geol.* **2005**, *218*, 339–359. [[CrossRef](#)]
88. Zhang, Q.; Wang, Y.; Li, C.D.; Wang, Y.L.; Jin, W.J.; Jia, X.Q. Granite classification on the basis of Sr and Yb contents and its implications. *Acta Petrol. Sin.* **2006**, *22*, 2249–2269. (In Chinese with English abstract)
89. Cui, J.W.; Tang, Z.M.; Deng, J.F.; Yue, Y.J.; Meng, L.S.; Yu, Q.F.; Li, J.X.; Lai, S.C.; Qi, L.; Guo, G.C.; et al. *Altyn Tagh Fault System*; Geological Publishing House: Beijing, China, 1999; pp. 39–49. (In Chinese)
90. Ma, T.Q.; Wang, X.H. Characteristic and geology meaning of alkaline calcium invade-rock zone at the SW Fringe of Altun Massif. *Hunan Geol.* **2002**, *21*, 12–16. (In Chinese with English abstract)
91. Liu, L.; Che, Z.C.; Wang, Y.; Luo, J.H.; Wang, J.Q.; Gao, Z.J. The evidence of Sm-Nd isochron age for the early Paleozoic ophiolite in Mangya area, Altun Mountains. *Chin. Sci. Bull.* **1998**, *43*, 754–756. (In Chinese with English abstract) [[CrossRef](#)]
92. Yang, J.S.; Shi, R.D.; Wu, C.L.; Su, D.C.; Chen, S.Y.; Wang, X.B.; Woonden, J. Petrology and SHRIMP age of the Hongliugou ophiolite at Milan, north Altun, at the northern margin of the Tibetan plateau. *Acta Petrol. Sin.* **2008**, *24*, 1567–1584. (In Chinese with English abstract)
93. Liu, L.; Wang, C.; Cao, Y.T.; Chen, D.L.; Kang, L.; Yang, W.Q.; Zhu, X.H. Geochronology of multi-stage metamorphic events: Constraints on episodic zircon growth from the UHP eclogite in the South Altyn, NW China. *Lithos* **2012**, *136*, 10–26. [[CrossRef](#)]
94. Liu, L.; Wang, C.; Chen, D.L.; Zhang, A.D.; Luo, J.H. Petrology and geochronology of HP–UHP rocks from the South Altyn Tagh, northwestern China. *J. Asian Earth Sci.* **2009**, *35*, 232–244. [[CrossRef](#)]
95. Yang, J.S.; Xu, Z.Q.; Zhang, J.X.; Sun, S.G.; Wu, C.L.; Shi, R.D.; Li, H.B.; Maurice, B. Early Paleozoic North Qaidam UHP metamorphic belt on the north-eastern Tibetan plateau and a paired subduction model. *Terra Nova* **2002**, *14*, 397–404.
96. Wu, C.L.; Wooden, J.L.; Robinson, P.T.; Gao, Y.H.; Wu, S.P. Geochemistry and zircon SHRIMP U-Pb dating of granitoids from the west segment of the North Qaidam. *Sci. China Earth Sci.* **2009**, *52*, 1771–1790. (In Chinese with English abstract) [[CrossRef](#)]
97. Hao, G.J.; Lu, S.N.; Wang, H.C.; Xin, H.T.; Li, H.K. The pre-Devonian tectonic framework in the northern margin of Qaidam basin and geological evolution of Olongbuluck palaeo block. *Earth Sci. Front.* **2004**, *11*, 115–122. (In Chinese with English abstract)
98. Ge, X.H.; Ye, H.W.; Liu, Y.J.; Liu, J.L.; Pan, H.X.; Ren, S.M. Research Progress of Altyn Fault In Western China. *Earth Sci. Front.* **2000**, *7*, 243–244. (In Chinese with English abstract)
99. Chen, X.H.; Gehrels, G.; Wang, X.F.; Yang, F.; Chen, Z.L. Granite from north Altyn Tagh, NW China: U-Pb geochronology and tectonic setting. *Bull. Mineral. Petrol. Geochem.* **2003**, *22*, 294–298. (In Chinese with English abstract)
100. Zuo, G.C.; Liu, J.C. The evolution of tectonic of early Paleozoic in north Qilian range, China. *Sci. Geol. Sin.* **1987**, *1*, 14–24. (In Chinese with English abstract)
101. Feng, Y.M.; He, S.P. *Geotectonics and Orogeny of the Qilian Mountains, China*; Geological Publishing House: Beijing, China, 1996; pp. 84–101. (In Chinese)
102. Wilde, S.A.; Zhao, G.; Sun, M. Development of the North China Craton during the late Archaean and its final amalgamation at 1.8 Ga: Some speculations on its position within a global Palaeoproterozoic supercontinent. *Gondwana Res.* **2002**, *5*, 85–94. [[CrossRef](#)]
103. Wang, Z.Q.; Jiang, C.F.; Yan, Q.R.; Yan, Z. Accretion and collision orogenesis in the West Kunlun Mountains. China. *Gondwana Res.* **2001**, *4*, 843–844.
104. Tung, K.; Yang, H.J.; Yang, H.Y.; Liu, D.; Zhang, J.; Wan, Y.; Tseng, C.Y. SHRIMP U-Pb geochronology of the zircons from the Precambrian basement of the Qilian Block and its geological significances. *Chin. Sci. Bull.* **2007**, *52*, 2687–2701. (In Chinese with English abstract) [[CrossRef](#)]
105. Zhu, B.Q. Geochemical evidence for the southern China block being a part of Gondwana. *J. Southeast Asia Sci.* **1994**, *9*, 319–329.
106. Wu, F.Y.; Zhao, G.C.; Wilde, S.A.; Sun, D. Nd isotopic constraints on crustal formation in the north China craton. *J. Asian Earth Sci.* **2005**, *24*, 523–545. [[CrossRef](#)]

Disclaimer/Publisher’s Note: The statements, opinions and data contained in all publications are solely those of the individual author(s) and contributor(s) and not of MDPI and/or the editor(s). MDPI and/or the editor(s) disclaim responsibility for any injury to people or property resulting from any ideas, methods, instructions or products referred to in the content.